

1 **Consequences of inhibition of mixed-layer deepening by the**
2 **West India Coastal Current for winter phytoplankton bloom in**
3 **the northeastern Arabian Sea**

4 **V. Vijith¹, P. N. Vinayachandran¹, V. Thushara¹, P. Amol¹, D. Shankar², A. C. Anil²**

5 ¹Centre for Atmospheric and Oceanic Sciences, Indian Institute of Science, Bangalore, Karnataka, India

6 ²CSIR-National Institute of Oceanography, Dona Paula, Goa, India

7 **Key Points:**

- 8 • West India Coastal Current inhibits entrainment of nutrients in the north-
9 eastern Arabian Sea
- 10 • Chlorophyll is lower in the southern part of the northeastern Arabian Sea
11 compared to the northern part
- 12 • Evidence of coastal Kelvin waves influencing biology in the north Indian
13 Ocean

Abstract

The intense winter phytoplankton bloom during November – February in the northeastern Arabian Sea (NEAS) was thought, until recently, to be controlled only by a convective deepening of the mixed layer (ML) owing to cool and dry northeasterlies. But, a recent study has shown that the deepening of the ML in the southern NEAS is inhibited by the poleward advection of low-salinity water from the south by the West India Coastal Current (WICC). Using an Ocean General Circulation Model coupled with an ecosystem model, we investigate the consequences of the inhibition of mixed-layer deepening for winter phytoplankton bloom in the NEAS. We show that, during the winter monsoon, the shallow ML inhibits the entrainment of nutrients in the southern NEAS. Strong (weak) positive nitrate tendency in the northern (southern) NEAS seen in the model during the winter monsoon is maintained by strong (weak) entrainment. As a result, the chlorophyll integrated to 200 m depth from the surface is lower in the southern NEAS than in the northern NEAS. The inhibition of mixed-layer deepening in the south affects the size-based distribution of small and large phytoplankton, nutrient limitation terms and growth rate, and their elemental composition. The WICC, which inhibits the deepening of the ML and affects the winter bloom in the NEAS, is driven by coastal Kelvin waves generated by remote winds. This paper demonstrates a mechanism by which remotely forced coastal Kelvin waves impact the biology in the north Indian Ocean.

1 Introduction

There are two distinct phytoplankton blooming seasons in the northeastern Arabian Sea (NEAS; Figure 1 shows the region of interest: 18°N–25.5°N and 64°E–72°E), one of the most productive regions in the north Indian Ocean (NIO; north of 5°S). The first seasonal bloom occurs during the summer monsoon (June – September), when the climatological winds are southwesterly. The second occurs about a month later, during the winter monsoon (November – February), when the winds reverse and blow from the northeast. The summer bloom is attributed to upwelling of cold, nutrient rich sub-surface water [Banse, 1968, 1987; Lévy *et al.*, 2007; Mc-

44 *Creary et al.*, 2009]. Several studies based on observation [*Banse*, 1968, 1984;
45 *Banse and McClain*, 1986; *Banse and English*, 1993; *Madhupratap et al.*, 1996]
46 and modelling [*Lévy et al.*, 2007; *McCreary et al.*, 2009; *Koné et al.*, 2009] de-
47 clare that entrainment of nutrients, owing to deepening of the mixed layer (ML)
48 forced by convective cooling at the surface of the ocean and, often referred to as
49 winter cooling, is the mechanism behind winter blooming.

50 A recent study by *Shankar et al.* [2015] has recognized that, during the win-
51 ter monsoon, maximum convection marked by maximum net heat flux is observed
52 in the southern section of the NEAS, whereas the maximum mixed layer depth
53 (MLD) is observed in the northern part. They showed that the formation of a deep
54 ML in the southern NEAS is inhibited by the poleward advection of low-salinity
55 water by the West India Coastal Current (WICC). Briefly, they concluded that ad-
56 vection by the WICC plays a significant role in determining MLD variations, and,
57 by extension, the ecosystem dynamics in the NEAS.

58 The recent findings by *Shankar et al.* [2015] have motivated us to investi-
59 gate the biological consequences of the inhibition of ML deepening in the NEAS.
60 However, apart from satellite derived chlorophyll and climatological atlases (for
61 example, World Ocean Atlas [*Garcia et al.*, 2014]), the data on chlorophyll and
62 nutrient distribution in the NEAS are too sparse to conduct such an investigation.
63 Numerical modelling is the only available tool to address this issue. Therefore,
64 we utilize a coupled physical-ecosystem model of the Indian Ocean to investi-
65 gate the consequences of the inhibition of ML deepening in the NEAS by the WICC.

66 Yet another motivation is that the WICC that inhibits the ML deepening in
67 the NEAS is remotely forced. The monthly-mean alongshore winds along the west
68 coast of India are equatorward throughout the year [*Shetye et al.*, 1985], but the
69 WICC flows against the winds, i.e., poleward, during the winter monsoon [*Banse*,
70 1968; *Shetye et al.*, 1991]. Theoretical studies of the NIO using linear models [*Mc-*
71 *Creary et al.*, 1993; *Shankar and Shetye*, 1997; *Shankar et al.*, 2002] showed that
72 the seasonal cycle of the WICC is forced by winds remote to the region of inter-
73 est (the west or east coast of India). These remote winds off the Indian coast force
74 coastal Kelvin waves and drive the coastal circulation. The WICC during the win-

75 ter monsoon is driven by downwelling coastal Kelvin waves generated by winds
76 off Sri Lanka and the east coast of India. In essence, the majority of the oceanographic
77 processes along the coast of India cannot be interpreted solely based on
78 local processes [McCreary *et al.*, 1993; Shankar and Shetye, 1997; Shankar *et al.*,
79 2002; Shetye *et al.*, 2008]. It is, therefore, crucial to understand how the coastal
80 Kelvin waves influence the biology of the NIO. The NEAS is a region suitable
81 for this study as a considerable understanding of how the remotely-driven WICC
82 influence MLD variations already exist [Shankar *et al.*, 2015].

83 The organization of the paper is as follows. The next section summarises
84 the relevant observational and theoretical background and lists the specific ob-
85 jectives of this paper. Section 3 presents a coupled Ocean General Circulation
86 Model (OGCM)-ecosystem model of the Indian Ocean. Section 4 presents the
87 model results and Section 5 discusses them. A summary of the paper is given in
88 Section 6. Two phrases - the northern NEAS and the southern NEAS, recur through-
89 out this paper. Nevertheless, we do not identify a physical boundary that delin-
90 eates the north and the south. Perhaps a possible marker is the salinity contour
91 of 36.2 psu, which intrudes to approximately 23°N by February (Figure 1). Equator-
92 ward of this contour, the deepening of the ML is inhibited in the NEAS. For
93 our analysis, we consider two 1° × 1° boxes near the 1000 m isobath at 24°N
94 and 19°N, as respectively representing the northern and southern NEAS. It may
95 also be noted that we have not included in our study the continental shelf region,
96 where the chlorophyll concentration is exceedingly high. We will be addressing
97 the region seaward of the 1000 m isobath.

98 **2 Background**

99 **2.1 Oceanographic setting of the NEAS**

100 During the International Indian Ocean Expedition (IIOE; 1959–65), it was
101 noticed that sinking of cool, high-saline water occurs during November off Karachi
102 in the NEAS [Banse, 1968], and provided the earliest evidence for convective mix-
103 ing during winter in the NEAS. The cool, dry winds that blow from the north-
104 east increase the latent heat flux over the NEAS and cause increased evaporation

105 at the surface. Consequently, the surface salinity in the NEAS increases to more
106 than 36.5 psu (Figure 2c), resulting in the formation of a high-salinity water mass,
107 called the Arabian Sea High-Salinity Water mass [Rochford, 1964; McCreary *et al.*,
108 1993; Prasad and Ikeda, 2002a,b; Jain *et al.*, 2016]. The evaporation also decreases
109 the sea surface temperature from more than 28° C in the north in November to
110 less than 25° C in February (Figure 2a). A detailed review of the oceanographic
111 setting of the NEAS is available in Shankar *et al.* [2015].

112 The WICC is the major coastal current in the eastern Arabian Sea. The core
113 of the WICC lies mainly along the 1000 m isobath. The typical current speed as-
114 sociated with the WICC in the NEAS during the winter monsoon is approximately
115 0.1–0.2 m s⁻¹ (Figure 2e). The WICC flows poleward against the alongshore
116 component of the wind stress during the winter monsoon and reverses its direc-
117 tion during the summer monsoon [Shetye *et al.*, 1990, 1991; Schott and McCreary,
118 2001]. Amol *et al.* [2014] have given a detailed description of the seasonal and
119 intraseasonal variability of the WICC.

120 **2.2 Inhibition of deepening of mixed layer**

121 The evolution of MLD in the NEAS during the winter monsoon (computed
122 from the North Indian Ocean Atlas (NIOA) prepared by Chatterjee *et al.* [2012])
123 is shown in Figure 2g. The MLD in the northern NEAS, which is around 20–30
124 m during November, deepens to more than 120 m by January. The deep ML in
125 the northern NEAS is maintained through February. However, in the southern NEAS,
126 the deepening of the ML is not as intense as in the north; the deepest MLD in Jan-
127 uary is only 40–50 m and it shallows to 20–30 m by February.

128 Naqvi *et al.* [2006] stated that the deepening of the ML is not uniform in the
129 NEAS and identified the intrusion of fresher and warmer water from the south
130 as a cause. Also, an Indian Ocean model simulation by Han *et al.* [2001] suggested
131 that the effects of evaporation on MLD are not uniform in the NEAS. However,
132 neither of these studies quantified the interplay of physical processes that deter-
133 mine the evolution of the ML in the NEAS, which was described by Shankar *et al.*
134 [2015]. Though the region of high latent heat flux and net heat flux occurs in the

135 southern NEAS, the deep MLs occur in the north. The deepening of the ML in
136 the south by convective cooling at the surface owing to high latent heat flux is in-
137 hibited by low-saline water (< 35.5) advected by the WICC and deep MLs are,
138 therefore, restricted to the north of $22\text{--}23^\circ\text{N}$. The deepening of the ML in the north
139 is sustained in February as the convective mixing happens before the arrival of
140 the low-salinity water. The reader is referred to *Shankar et al.* [2015] for more
141 details on the dynamics of the inhibition of the ML in the NEAS.

142 **2.3 Climatology of nutrients**

143 Nitrate (NO_3) is the most limiting nutrient in this region [*Wiggert et al.*, 2006;
144 *Koné et al.*, 2009] and iron (Fe) is replete [*Wiggert et al.*, 2006; *Naqvi et al.*, 2010].
145 Observations carried out south of the NEAS in February 1995 [*Madhupratap et al.*,
146 1996] had shown that the $2 \mu\text{mol kg}^{-1}$ contour of NO_3 , which was at a depth of
147 30 m at 13°N , rose to the surface at 16°N along 64°E . North of 16°N , NO_3 con-
148 centrations was . more than $2 \mu\text{mol kg}^{-1}$. NO_3 of about $2 \mu\text{mol kg}^{-1}$ were re-
149 ported in the NEAS during winter [*Roy et al.*, 2015; *Balachandran et al.*, 2008;
150 *Naqvi et al.*, 2002]. The predominant contribution to vertically integrated NO_3
151 pool during winter is from vertical diffusion, including convective and turbulent
152 (based on the modelling study by *Koné et al.* [2009]).

153 Average values of phosphate (PO_4) and silicate (SiO_4) in the ML during win-
154 ter in the NEAS are 1 and $4 \mu\text{mol kg}^{-1}$, respectively [*Roy et al.*, 2015]. PO_4 data
155 collected on-board R/V Anton Bruun during IIOE [*Anonymous*, 1965] showed
156 that along the 180 m isobath, PO_4 concentration increased from the south (0.1
157 $\mu\text{mol kg}^{-1}$ at 20°N) to the north ($0.6 \mu\text{mol kg}^{-1}$ at 24.8°N) during November.
158 *Naqvi et al.* [2002] reported that the water was rich in NO_3 and PO_4 , and depleted
159 in SiO_4 ($< 1 \mu\text{mol kg}^{-1}$), leading to a diatom limitation. They also reported that
160 the concentration of ammonium (NH_4) was below the detection limit ($< 0.2 \mu\text{mol}$
161 kg^{-1}).

162 Monthly climatological distribution of NO_3 and PO_4 is available at 1° res-
163 olution, in the World Ocean Atlas [*Garcia et al.*, 2014]. However, the number of
164 observations available in this region during winter is too sparse (see Figure S1

165 in the supporting information) to build any reliable inference related to the spatio-
166 temporal distribution of nutrients. Surface patterns of NO_3 and PO_4 available in
167 the atlas, are shown in Figures 3a and c, respectively. Coherent with the pattern
168 of MLD, surface concentrations of NO_3 also increase as the MLD deepens in the
169 north from November ($< 0.5 \mu\text{mol kg}^{-1}$) to February ($2.5 \mu\text{mol kg}^{-1}$). The in-
170 crease is marginal in the south. A similar pattern is also shown by PO_4 . Never-
171 theless, there are a few conspicuous deviations in the atlas from what may be ex-
172 pected based on the MLD pattern. Notably, the NO_3 (PO_4) contours during Jan-
173 uary (December) show an increase (decrease) offshore.

174 **2.4 Climatology of chlorophyll**

175 The seasonality of phytoplankton chlorophyll in the northern Arabian Sea
176 was discussed using ship-based observations by *Banse* [1987], using Coastal Zone
177 Color Scanner preceding the SeaWiFS period by *Banse and McClain* [1986] and
178 *Banse and English* [1993, 2000]. The timing of the onset of the winter bloom has
179 been documented by *Lévy et al.* [2007] using SeaWiFS data, and by *Koné et al.*
180 [2009] using a coupled OGCM-biogeochemical model. These studies estimated
181 that the onset occurs in the southern NEAS during October and is delayed un-
182 til January in the northern region of the NEAS. Winter phytoplankton produc-
183 tivity ends by March as the nutrient supply from below the ML is cut off [*Banse,*
184 1968] owing to surface heating and resulting shallowing of the ML.

185 Satellite-derived chlorophyll data show (Figure 3e) that, within the NEAS,
186 there is a regional difference in chlorophyll distribution throughout the winter with
187 the southern NEAS always having lower chlorophyll concentrations. This dif-
188 ference was first identified by *Banse and McClain* [1986] using satellite-derived
189 chlorophyll data. They recorded that large blooms were common north of 20°N ,
190 particularly in late winter. There is an increase in chlorophyll from November
191 to February in both the north and south.

2.5 Objectives of the paper

Shankar et al. [2015] proposed that the inhibition of ML deepening in the south of the NEAS by the WICC can play a significant role in determining chlorophyll concentrations and ecosystem dynamics. Our analysis presented in the earlier part of this section suggests that this hypothesis may be valid. To validate this hypothesis, we use a coupled physical-biological model. The model is expected to reproduce higher nutrient levels in the north, where the ML is deep, compared to the south, where the ML is shallow. We, then, present a detailed analysis of the model simulated nutrients and chlorophyll. This includes a description of the vertical section along the 1000 m isobath, as in *Shankar et al.* [2015], and the time-series of physical and biological variables. We, subsequently, estimate different terms of the NO_3 budget and show the inhibition of entrainment in the south. Finally, we address the consequences of ML inhibition on three specific issues: nutrient limitation terms, distribution of different classes of phytoplankton (small and large), and their elemental composition (for example, N:P ratio).

3 The ecosystem model

The physical model used in this paper is a quarter degree resolution, free surface, hydrostatic, z -coordinate model of the Indian Ocean based on the Modular Ocean Model (MOM4p1) [*Griffies*, 2009]. The set up of the physical model is similar to that in *Kurian and Vinayachandran* [2007], *Vinayachandran et al.* [2007], *Chatterjee et al.* [2013] and *Shankar et al.* [2015]. The model domain extends from 30°S to 30°N and from 30°E to 120°E and has 40 vertical levels, with 25 levels in the top 200 m. The model has a vertical resolution of 5 m in the top 60 m. The vertical mixing is based on *Large et al.* [1994]. A combination of biharmonic friction with Smagorinsky viscosity and Laplacian mixing is used in the horizontal direction [*Griffies and Hallberg*, 2000]. Advection of salinity and temperature is based on Multi-dimensional Piecewise Parabolic Method (MDPPM). Penetrative shortwave heating is prescribed in the top 100 m following *Morel and Antoine* [1994]. The model was forced with climatological winds, precipitation and river discharge. The latent, sensible and longwave heat fluxes are calculated

222 by the model as a function of SST. Winds were based on a 3-hour merged wind
 223 product with the high frequency component (period less than 36 hours) from the
 224 ECMWF reanalysis (ERA-INTERIM) and the low-frequency component from
 225 QuikSCAT. The 3-hour radiative fluxes available from ERA were used. Precip-
 226 itation is taken from the Tropical Rainfall Measuring Mission (TRMM). River
 227 discharge is based on climatological data from *Vôrdsmarty et al.* [1996] and is
 228 prescribed within the top 15 m. The model was initialised using temperature and
 229 salinity data from the World Ocean Atlas [*Locarnini et al.*, 2010; *Antonov et al.*,
 230 2010]. Table S1 in the supporting information gives a summary of the data used
 231 to force the model and their sources.

232 The ecosystem model used in this paper is based on the Tracers of Phyto-
 233 plankton with Allometric Zooplankton (TOPAZ), a module that can be coupled
 234 with the MOM. TOPAZ is a widely used ecosystem model. It has been success-
 235 fully employed to investigate ecosystem variability associated with ENSO [*Park*
 236 *et al.*, 2014], Indian Ocean Dipole [*Park and Kug*, 2014], evolution of chlorophyll
 237 in the northwestern Arabian Sea [*Marvasti et al.*, 2015] and the northern Atlantic
 238 [*Pastor et al.*, 2013]. TOPAZ represents all the major nutrients or species (car-
 239 bon, nitrate, ammonium, phosphate, silicate, dissolved oxygen, iron and calcium
 240 carbonate) and three phytoplankton groups: diazotrophs (cyanobacteria), small
 241 (picoplankton and nanoplankton) and large (diatoms and algae) phytoplankton.
 242 Total chlorophyll, in the model, is calculated as the sum of chlorophyll in each
 243 of the three groups of phytoplankton. The model has a total of 25 tracers and in-
 244 cludes processes such as the atmospheric deposition of iron, nitrification and den-
 245 itrification. *Dunne et al.* [2010] give a detailed documentation of TOPAZ. The
 246 set up of the ecosystem model is similar to that in *Gnanadesikan et al.* [2011].

247 The growth rate of each phytoplankton group in the model is limited by tem-
 248 perature, whatever nutrient is most limiting among N, P and Fe, and by light. The
 249 growth rate of each phytoplankton group is given by

$$\mu = \frac{P_{max}^C}{1 + \zeta} e^{\kappa T} \min(Lim_N, Lim_P, Lim_{Fe}) \times Lim_{Irr} . \quad (1)$$

250 Here, P_{max}^C is the maximum carbon assimilation rate of each group of phytoplank-
 251 ton, ζ is the cost of biosynthesis (set to 0.1, taken from *Geider et al.* [1997]), κ

252 is the Eppley temperature coefficient (0.063), T is the temperature and Lim_N ,
 253 Lim_P , Lim_{Fe} and Lim_{Irr} refer to limitation terms for nitrogen, phosphorus, iron,
 254 and light, respectively. The $min(Lim_N, Lim_P, Lim_{Fe})$ is called the Liebig lim-
 255 itation term.

256 The limitation term of nitrogen in TOPAZ is given by

$$Lim_N = \frac{NO_3}{k_{NO_3} + NO_3(1 + NH_4/k_{NH_4})} + \frac{NH_4}{k_{NH_4} + NH_4}. \quad (2)$$

257 Here, k_{NO_3} and k_{NH_4} are half-saturation constants of NO_3 and NH_4 respec-
 258 tively. The first and second terms on the right-hand side of Equation 1 are the lim-
 259 itation terms for NO_3 and NH_4 , respectively. The limitation terms for PO_4 and
 260 dissolved iron (Fe) are based on the Michaelis-Menton formulation [*Michaelis*
 261 *and Menten*, 1913] as given below.

$$Lim_C = \frac{C}{k_C + C}. \quad (3)$$

262 Here C denotes PO_4 or Fe.

263 The light limitation term in the model is given by

$$Lim_{Irr} = 1 - e^{-\alpha\theta\frac{I}{P_N^C}}. \quad (4)$$

264 Here, α is the initial slope of chlorophyll-specific response curve of photosyn-
 265 thesis versus light. θ is the ratio of chlorophyll to carbon of each phytoplankton
 266 group. P_N^C is the nutrient limited carbon assimilation rate. The vertical variation
 267 of chlorophyll depends on the availability of light due to variations in solar in-
 268 solation and MLD. This variation is imposed by using a depth-dependent θ . The
 269 formulation of θ in the model is given by

$$\theta = \theta_{min}min(Lim_N, Lim_P, Lim_{Fe}) + \frac{\theta_{max} - \theta_{min}}{1 + \alpha(\theta_{max} - \theta_{min})I/2P_N^C}. \quad (5)$$

270 Equation 5 implies that as the concentration of nutrients increase or the light de-
 271 creases the ratio of chlorophyll to carbon increases to match the increased need
 272 for light. Therefore, an increase in the ratio of chlorophyll to carbon does not nec-
 273 essarily mean an increase in biomass.

274 The grazing in TOPAZ is based on *Dunne et al.* [2005]. Grazing of diazotrophs
 275 and small phytoplankton are proportional to square of their concentration and large

276 phytoplankton is proportional to their concentration raised to the power of $4/3^{rd}$.
277 Furthermore, a Michaelis-Menton type threshold of minimum phytoplankton con-
278 centration is added to prevent phytoplankton from becoming extinct.

279 A summary of half-saturation coefficients, chlorophyll to carbon ratios, car-
280 bon assimilation rates, constant of phytoplankton grazing rate and remineralisa-
281 tion depth used in the ecosystem model is available in the supporting informa-
282 tion (Table S2). Sources of data used to initialize the model are listed in Table
283 S3 [*Locarnini et al.*, 2010; *Antonov et al.*, 2010; *Garcia et al.*, 2010].

284 The small phytoplankton in the model are weakly limited by nutrients (low
285 half-saturation coefficient), but are strongly limited by grazing; whereas the large
286 phytoplankton require more nutrients, but are less limited by grazing. Iron lim-
287 itation was applied only to diazotrophs, which are nitrogen fixers. Diazotrophs
288 represent a negligible fraction of biomass and are, hence, ignored in the rest of
289 this paper. The results presented in this paper were by imposing limitations due
290 to N and P. Two additional sensitivity tests were carried out imposing limitation
291 due to dissolved Fe for small and large phytoplankton, and SiO_4 for large phy-
292 toplankton. The former gave an unrealistically low chlorophyll in the north in Jan-
293 uary and February, which was not consistent with satellite-derived chlorophyll,
294 and the latter did not result in any noticeable change in the simulation.

295 The uptake of PO_4 is based on dynamic N:P stoichiometry [*Klausmeier et al.*,
296 2004]. PO_4 is allocated mainly to two classes of machinery, assembly and up-
297 take. The rate of assembly is proportional to the Liebig term and the rate of up-
298 take is proportional to $[1 - \min(\text{Liebig term})]$. Thus, during an exponential growth
299 rate, phytoplankton tends to assemble additional PO_4 , but less PO_4 during an op-
300 timum growth rate. This results in a lower N:P ratio during a higher growth rate
301 than during a lower growth rate.

302 The nutrients in the ecosystem model were initialised using the World Ocean
303 Atlas [*Garcia et al.*, 2010]. The physical model was run for 10 years with clima-
304 tological forcings and the coupled-physical-ecosystem model was subsequently
305 run for another 10 years. The output of the final year's simulation is used in this

306 paper as a climatological simulation. The simulation is validated by comparing
307 it with monthly climatological data in the following section. The climatological
308 data used for validating the SST are taken from a merged product of the TRMM
309 Microwave Imager and the Advanced Microwave Scanning Radiometer (TMI-
310 AMSRE), the SSS are taken from the NIOA, the currents are taken from Ocean
311 Surface Current Analysis Realtime (OSCAR; *Bonjean and Lagerloef* [2002]),
312 NO_3 and PO_4 are taken from *Garcia et al.* [2014] and chlorophyll is taken from
313 SeaWiFS. The climatological MLD is computed from the NIOA using a density
314 criterion, defined as the depth at which the density increases from the surface by
315 a value that corresponds to a decrease in temperature of 0.5°C [*Shenoi et al.*, 2004].
316 The model MLD is based on a buoyancy difference of $3 \times 10^{-4} \text{ m s}^{-2}$ with re-
317 spect to the surface level [*Kurian and Vinayachandran*, 2007]. A table listing the
318 sources of data used for validating the model [*Chatterjee et al.*, 2012; *Bonjean*
319 *and Lagerloef*, 2002; *Garcia et al.*, 2014] is given in the supporting information
320 (Table S4).

321 4 Results

322 4.1 Validation of the model

323 A respectable physical-biological model of the NEAS should replicate the
324 features seen in the observations noted in Section 2 and in *Shankar et al.* [2015].
325 These features are summarised below.

- 326 1. The model should reproduce the progressive cooling of the SST in the north-
327 ern NEAS and the intrusion of low-salinity water in the south as the win-
328 ter season progresses from November to February.
- 329 2. The WICC in the model should flow poleward with the core of the current
330 lying approximately along the 1000 m isobath as discussed in Section 2.1.
- 331 3. The model should reproduce the contrasting characteristics of the north and
332 south in the evolution of the ML as discussed in Section 2.2.
- 333 4. The model should have high concentrations of nutrients and chlorophyll
334 in the northern NEAS compared to the southern NEAS, as seen in *Garcia*
335 *et al.* [2014] and discussed in Sections 2.3 and 2.4.

336 In Figures 2 and 3, the model variables are compared with the climatology
337 of available observations. The figures show that the four conditions listed above
338 are fulfilled by the model. However, there are three major deviations from the ob-
339 served climatology. First, compared to the observed climatology, the model tem-
340 perature is cooler approximately by 1° C and salinity is fresher by 0.2 to 0.4 psu
341 at the surface. The stratification in the model is not affected by this difference and
342 is simulated well as the change in density owing to the negative salinity bias is
343 compensated by the negative temperature bias. Therefore, as observed, the model
344 MLD is deeper in the northern NEAS than in the southern NEAS. Second, the
345 model marginally overestimates NO₃ and underestimates PO₄. Unlike in *Garcia*
346 *et al.* [2014], the model suggests concentrations of NO₃ and PO₄ as being con-
347 sistentally higher in the northern NEAS than in south. The offshore decrease of NO₃
348 during January seen in *Garcia et al.* [2014] (which may be an artefact of data gaps)
349 is absent in the model (Figure 3a-b). Third, the chlorophyll in the model is weaker
350 than the satellite-derived chlorophyll. Nevertheless, the simulated patterns are
351 consistent with the observations and are adequate for the research reported in this
352 paper.

353 **4.2 Vertical section and time series**

354 A description of vertical structure and time series of nutrients and chloro-
355 phyll was omitted in Section 2.3. A reliable description of this kind cannot be made
356 owing to the sparsity of data based on observations. We, therefore, resort to the
357 model simulation to describe the evolution of temperature, salinity, alongshore
358 currents, nutrients and chlorophyll using the vertical section (Figure 4) and the
359 time-series along the 1000 m isobath (Figure 5), and the time-series showing the
360 evolution of vertical structure at the centres of the northern box (24°N) and the
361 southern box (19°N) (Figure 6).

362 The modelled alongshore component of WICC, which flows poleward through-
363 out the winter, is strongest in December with a speed of 0.15 m s⁻¹ near the sur-
364 face (Figure 4c). Advected by the WICC, low-salinity water progressively intrudes
365 into the NEAS (Figures 4b and 5b). A 0.5 psu drop in the modelled SSS is seen

366 at 19°N during mid-December, whereas the SSS increases only marginally at 24°N
367 (Figures 5d and 6d). 35.5 psu isohaline appears in the southern NEAS near the
368 surface in December and intrudes about 400 km northwards to about 21°N by Febru-
369 ary (Figure 4b and 5b). South of 35.5 psu isohaline, the deepening of the ML is
370 inhibited (Figure 4b). In March, the WICC weakens and reverses its direction,
371 and flows equatorward (Figure 5c).

372 At 24°N, the modelled SST decreases from 27° C in November to 23° C in
373 February (Figures 5b and 6b). Owing to the cooling at the surface, the mixed layer
374 deepens by an order of magnitude, from 20 m in November to 140 m in Febru-
375 ary whereas the MLD at 19°N deepens only from 25 m in November to 60 m in
376 February (Figure 5h). As the ML deepens in the north, cold sub-surface water
377 that is rich in NO_3 and PO_4 entrains to the ML (Figures 4a,d and e). Vertical sec-
378 tions of the nutrients (Figure 4d-e) resemble the temperature sections (Figure 4a).
379 The $2 \mu\text{mol kg}^{-1}$ contour of NO_3 which is at a depth of 30 – 40 m at 21°N in
380 November rises to the surface in January (Figure 4d). North of this latitude, the
381 concentrations are higher, and south of this latitude the entrainment of NO_3 and
382 PO_4 is limited.

383 The temporal evolution of the modelled nutrients (Figure 5i-l) is reminis-
384 cent of the evolution of the ML. NO_3 (PO_4) increase from near zero ($< 0.1 \mu\text{mol}$
385 kg^{-1}) in November to $6 \mu\text{mol kg}^{-1}$ ($0.6 \mu\text{mol kg}^{-1}$) in February, at 24°N (Fig-
386 ures 6h and j), whereas at 19°N, the increase is marginal (Figures 6g and i). At
387 24°N, the depth-integrated chlorophyll in the top 200 m of the water column in-
388 creases by threefold from $30 \mu\text{g m kg}^{-1}$ in November to $90 \mu\text{g m kg}^{-1}$ in Febru-
389 ary (Figure 5n). At 19°N, the depth-integrated chlorophyll remains between 30–
390 $50 \mu\text{g m kg}^{-1}$ throughout the winter. Figure 5m shows that a north-south gradi-
391 ent of chlorophyll is persistently seen from mid-December to the end of Febru-
392 ary.

393 A notable feature in the vertical section of the modelled chlorophyll is the
394 presence of a distinct subsurface chlorophyll maximum (Figures 4f, and 6k and
395 l) lying within the ML throughout the season. Though the vertical density struc-
396 ture is well-mixed in the ML, along with ample amount of nitrates and phosphates

397 (Figures 4 and 6), the variability in light and grazing, maintains the depth of sub-
398 surface chlorophyll maximum within the lower ML.

399 Peaks of NO_3 and PO_4 occur on 7 January at 19°N and 35 days later, on 11
400 February, at 24°N (Figure 5j and l). Interestingly, these peaks do not coincide with
401 the peaks in the MLD, which peaks during the first week of February at 19°N and
402 24°N (Figure 5h). Furthermore, the MLD does not decrease in the southern NEAS
403 as rapidly as it does in the northern NEAS. The chlorophyll peak at 19°N coin-
404 cides with the peak in the nutrients. The chlorophyll curve at 24°N attains its peak
405 during mid-January and sustains it till late February (Figure 5n). A second peak
406 observed in the chlorophyll, often referred to as a detrainment bloom [McCreary
407 *et al.*, 1996], occurs in the northern NEAS during the end of February. This bloom
408 arises from the availability of sufficient nutrients and light in the ML as it shal-
409 lows. Such a detrainment bloom is completely absent in the south at 19°N .

410 **4.3 Entrainment of NO_3**

411 Here, we investigate the budget of NO_3 in the ML (Figure 7) to assess the
412 pattern of entrainment that lends a significant contribution to the NO_3 balance equa-
413 tion. The physical terms in the budget, that is, tendency (rate of change), entrain-
414 ment and advection, were calculated based on *Vialard and Delecluse* [1998] and
415 the biological processes were saved from the model. In the northern NEAS (at
416 24°N), NO_3 shows a positive tendency (Figures 7a and b). After 11 February the
417 tendency becomes negative. In the south (at 19°N), the tendency is weakly pos-
418 itive till 7 January. These are the two days on which nutrients peak at 24°N and
419 19°N . The dominant component that balances the NO_3 tendency is entrainment
420 (Figures 7c and d). Entrainment is highest during December – January in the north
421 (at 24°N) when it reaches $\sim 0.2 \mu\text{mol kg}^{-1} \text{ day}^{-1}$ (Figure 7d). Entrainment in
422 the south is less than that in the north during this period. There is a period dur-
423 ing the second half of January when the entrainment in the south is higher than
424 in the north (Figure 7d) because the MLD attains its maximum in the south (Fig-
425 ure 5h).

426 Advection terms (Figures 7e–h) are on an average less than $0.05 \mu\text{mol kg}^{-1}$
427 day^{-1} and are not important in the NO_3 budget. At 19°N , both horizontal and
428 vertical advection terms (Figures 7f and h) remove NO_3 in the ML after 7 Jan-
429 uary. The net contribution from the biological processes (nitrification – denitri-
430 fication – uptake by phytoplankton) is shown in Figures 7i and j. The dominant
431 term in this is the uptake by phytoplankton. The negative tendency at 24°N from
432 11 February onwards (Figure 7b) is due to a decrease in entrainment (Figure 7d)
433 and an increase in uptake by phytoplankton (Figures 7i and j).

434 **4.4 Differences in physical processes between the northern and south-** 435 **ern NEAS**

436 The salient differences in physical processes between the northern and south-
437 ern NEAS that result in lower chlorophyll concentration in the southern NEAS
438 can be summarised as follows. In the northern NEAS, cool-dry-northeasterly winds
439 cause evaporation at the sea surface. Due to this evaporation, the SST at 24°N on
440 the 1000 m isobath decreases from 27°C in November to 23°C in February (Fig-
441 ures 5b and 6b). The cooling at the surface leads to convective mixing and the
442 ML monotonically deepens from 25 m in November to 140 m in February (Fig-
443 ure 5h and 6b). The SSS marginally increases by 0.1 psu (Figures 5d and 6d). The
444 convective mixing entrains nutrients to the ML (Figure 7c) resulting in a posi-
445 tive nutrient tendency from November till mid-February (Figure 7b). After mid-
446 February, the entrainment weakens (Figure 7d) and the uptake due to phytoplank-
447 ton increases (Figure 7j), leading to a negative NO_3 tendency (Figure 7b). The
448 MLD, NO_3 and PO_4 peak during mid-February (Figures 7f, j and l). Chlorophyll
449 peaks during mid-January and is sustained till the end of February (Figures 5n
450 and 6l).

451 In the southern NEAS, the poleward flowing WICC advects low-salinity wa-
452 ter (< 35.5 psu; Figures 5c and 6c) from the south and inhibits the deepening
453 of the ML. At 19°N , the SST decreases from 28°C in November to 25°C in Febru-
454 ary (Figures 5b and 6a). Unlike in the north, the SSS decreases from 35.8 psu in
455 November to 35.3 psu by the end of December (Figures 5b and 6c). The ML only

456 deepens from 25 m in November to 60 m in February (Figures 5h and 6a). Due
457 to the inhibition of ML deepening, the entrainment in the south is weak compared
458 to that in the north (Figure 7d). After the first week of January the NO_3 tendency
459 turns negative (Figure 7b) as advection (Figures 7f and h) and biological processes
460 (Figure 7j) remove NO_3 from the ML. The total chlorophyll in the water column
461 is less than half of that in the northern NEAS (Figure 5n). The peak of the chloro-
462 phyll curve occurs during the first week of January, approximately a month ear-
463 lier compared to 24°N and coinciding with peaks in NO_3 and PO_4 (Figures 5j,
464 l and n); chlorophyll decreases monotonously after the peak. So, not only is the
465 chlorophyll concentration higher in the north, but it is also sustained for almost
466 twice as long compared to the south. The second peak in chlorophyll seen in the
467 northern NEAS during the end of winter is also inhibited in the southern NEAS
468 by the WICC.

469 In the next subsection, we investigate how the distribution of small and large
470 phytoplankton and the growth rate, nutrient limitation and N:P ratio of small phy-
471 toplankton respond to these differences in physical processes.

472 **4.5 Biological consequences of inhibition of ML deepening**

473 ***4.5.1 Size based distribution of phytoplankton***

474 The NEAS, in the model, is dominated by small phytoplankton (Figures 8a
475 and c). More than 70% of the total chlorophyll is contributed by small phytoplank-
476 ton throughout the season. The pattern of distribution of small (Figure 8a) and
477 large phytoplankton (Figure 8c) is similar to the distribution of the total chloro-
478 phyll discussed in Section 4.2. That is, both small and large phytoplankton show
479 the north-south difference in their chlorophyll concentrations. As the nutrient lev-
480 els increase dramatically in the north (24°N) from November to February the small
481 phytoplankton show a sharp increase (Figure 8b). The large phytoplankton, which
482 require more nutrients, are fewer at 19°N (Figure 8d).

483 The detrainment bloom in the north during late February that was noted in
484 the Section 4.2 results from an increase in large phytoplankton (Figure 8c). This

485 bloom lasts for about a week and is restricted north of approximately 23°N. The
486 small phytoplankton do not respond to the detrainment event.

487 **4.5.2 Nutrient limitation and growth rate**

488 The nutrient limitations of NO_3 and PO_4 of small phytoplankton given by
489 Equations (2) and (3), respectively, are shown in Figures 9a and c. NO_3 , that has
490 the minimum value of the limitation term (Leibig term), is the most limiting nu-
491 trient in the NEAS. Therefore, the limitation term for NO_3 will determine the growth
492 rate of phytoplankton in the NEAS. By an extension from the distribution of nu-
493 trients, the limitation term is expected to be smaller in the south compared to the
494 north owing to the inhibition of the entrainment of NO_3 in the south. As the sea-
495 son progresses, the nutrient limitation terms increase in the NEAS. The limita-
496 tion terms reach a maximum during the first week of January at 19°N and dur-
497 ing the last week of February at 24°N (Figure 9b and d).

498 The spatial distribution of the growth rate (Equation 1) of small phytoplank-
499 ton in the surface level is shown in Figure 9e. The growth rate of small phyto-
500 plankton at 19°N increases from 0.8 day^{-1} in November to 1.6 day^{-1} in January
501 (Figure 9f). At 24°N, the growth rate increases from 1.2 day^{-1} in November to
502 2.0 day^{-1} in February. Similar to the vertical distribution of NO_3 and PO_4 (Fig-
503 ure 6 g-j), the Leibig term is also well mixed in the ML. As a result, the only term
504 that will determine the vertical structure of growth rate is the light limitation term
505 (see Equation 1). That is, the growth rate decreases vertically downward depend-
506 ing on the penetration of light.

507 **4.5.3 N:P stoichiometry**

508 TOPAZ allows for a dynamic N:P stoichiometry (refer to Section 3). In TOPAZ,
509 during an exponential growth rate, phytoplankton tend to assemble additional PO_4 ,
510 but less PO_4 during an optimum growth rate, resulting in a lower N:P ratio dur-
511 ing an exponential growth rate. The monthly distribution of the N:P ratio of small
512 phytoplankton at the surface in the NEAS is shown in Figure 9g. The north-south
513 contrast seen in all the previously analysed variables is also seen in the N:P ra-

514 tio. In the northern NEAS (24°N), where the growth rate is higher, the N:P ra-
515 tio decreases from about 16 in November to about 9 in February (Figure 9h). How-
516 ever, in the south (19°N), where the growth rate is lower, the N:P ratio decreases
517 from 16 in November to 13 in February.

518 **5 Discussion**

519 Do remotely forced coastal Kelvin waves impact biology in the coastal ocean?
520 An early attempt to address this question was carried out by *Mysak et al.* [1982].
521 They observed coherent signals in the temperature, salinity, sea level and the to-
522 tal number of fish (*Sockeye salmon*) caught, and the average weight per fish in
523 the northeast Pacific off the coast of central Canada, at interannual periods (5–
524 6 years). These signals were found to propagate northwards with a phase speed
525 of a baroclinic Kelvin wave. They speculated that the signals in temperature, salin-
526 ity and sea level which were associated with this long period of baroclinic Kelvin
527 wave could have affected the variability seen in the fish catch. However, the mech-
528 anism that links these waves with biology was not demonstrated.

529 An obvious mechanism of influence of coastal Kelvin waves on biology is
530 by way of inhibition or enhancement of upwelling. *Dickson et al.* [1980] showed
531 the enhancement of upwelling due to upwelling favourable coastal Kelvin waves
532 and its signatures in an increased distribution of mackerel eggs on the slope of
533 the Bay of Biscay. Another example of this mechanism, from the NIO, was given
534 by *Shankar and Shetye* [1997]. *Longhurst and Wooster* [1995] had noted that weak
535 upwelling along the southwest coast of India began in February, 2–3 months be-
536 fore the onset of upwelling favourable southwesterlies. This early upwelling is
537 driven by remotely forced coastal Kelvin waves that drive an upwelling favourable
538 equatorward current. The mechanism of upwelling along the west coast of In-
539 dia was first shown by *McCreary et al.* [1993], but the connection to *Longhurst*
540 *and Wooster* [1995] was made by *Shankar and Shetye* [1997]. In this paper, we
541 have demonstrated an alternative mechanism of impact of coastal Kelvin waves
542 on biology, in the form of the inhibition of ML deepening in the NEAS.

543 Since the model is forced with climatological fields, the intraseasonal (30–
544 90 days) variability is missing. *Amol et al.* [2014] noted that the strength of the
545 intraseasonal signal decreases poleward along the west coast of India. Therefore,
546 it may be a fair approximation to ignore this for the NEAS. However, the time
547 series of the alongshore component of the WICC and surface chlorophyll from
548 regions south of the NEAS, for example, off Goa (see Figure S2 in the support-
549 ing information), show consistent patterns even at intraseasonal periods. We, there-
550 fore, expect that impact of remotely forced waves on biology can be expected all
551 along the coast of India in all frequency bands. However, biologists often ignore
552 the role of these waves and tend to infer their results as forced only locally. The
553 implications of the remote forcing of the WICC were emphasised over two decades
554 ago [*McCreary et al.*, 1993; *Shankar and Shetye*, 1997] and it is time that its role
555 in ecosystem dynamics and biogeochemical cycling is recognised. As shown by
556 *Amol et al.* [2012], the impact of remote forcing in the eastern Arabian Sea is not
557 restricted to the slope and Kelvin waves. Remote forcing via shelf waves extends
558 to the inner shelf, with obvious implications for biogeochemistry and fisheries.

559 Our results are consistent with the available observations in the NEAS. The
560 dominance of picoplankton (small phytoplankton) was reported by *Roy et al.* [2015]
561 and *Naqvi et al.* [2002]. A time shift of 1–2 months in the onset of the winter
562 bloom between the northern and the southern NEAS was shown by *Lévy et al.*
563 [2007]. Our analysis of the growth rate of small phytoplankton shows that it first
564 peaks in the south and later in the north. The time gap between the occurrence
565 of the peak at 19°N and 24°N is 35 days, which is consistent with the finding by
566 *Lévy et al.* [2007]. However, such a delay is not prominently visible in the chloro-
567 phyll patterns in the model. Instead, the chlorophyll in the north attains its peak
568 a week after the peak occurs in the south and sustains it for a longer duration than
569 in the south. It is also known that phytoplankton adjust their stoichiometry from
570 3:1 at the top of the ML to 10:1 near the bottom of the ML to match the nutrient
571 supply [*Roy et al.*, 2015].

572 For the western Arabian Sea (west of 65° E), *Landry et al.* [1998] using ob-
573 servations, had estimated a growth rate of $0 - 1.5 \text{ day}^{-1}$ and a standard devia-

574 tion of 0.38 day^{-1} for the winter monsoon. The higher growth rate, in the NEAS,
575 calculated by our model ($\sim 2.2 \text{ day}^{-1}$ as seen in Figure 9e) is justifiable as this
576 region is more productive compared to the western Arabian Sea. Finally, the fast
577 decline of chlorophyll and nitrate at 24°N in March (shown in Figures 8 and 9a)
578 suggests that grazing losses built in the model are also realistic.

579 Nature is also expected to deviate from the idealised equations in the model.
580 An example for this, from the NEAS, was shown by *Roy and Anil* [2015]. They
581 showed that convective mixing in the northern Arabian Sea inhibits the growth
582 of *Prochlorococcus* owing to modifications in the physical environment, which
583 is contrary to our results. This is a level of complexity that is beyond the scope
584 of the current generation of ecosystem models like TOPAZ.

585 **6 Summary**

586 The Arabian Sea is more saline compared to the other basin in the NIO, the
587 Bay of Bengal, because of significantly lower precipitation, higher evaporation
588 and much less runoff. The seasonally reversing monsoon winds over the NIO pro-
589 duce seasonally reversing currents that exchange water between the two basins.
590 One such current is the WICC that takes low-salinity waters of the Bay of Ben-
591 gal into the Arabian Sea. As the current takes the waters poleward along the west
592 coast of India, the contrast between salinity of the waters of the current with am-
593 bient waters has an impact on mixed-layer physics. This impact in the NEAS was
594 discussed by *Shankar et al.* [2015]. They showed that the inhibition of ML deep-
595 ening in the south of the NEAS is forced by the advection of low-salinity water
596 by the poleward-flowing WICC.

597 In this paper, we have set up a coupled physical-biological model to inves-
598 tigate the consequences of the inhibition of ML in the NEAS. The model is able
599 to simulate the spatio-temporal variability of physical and biological variables
600 in the NEAS. Furthermore, we show that the inhibition of mixing in the south-
601 ern part of the NEAS results in the inhibition of entrainment of nutrients to the
602 ML as hypothesised by *Shankar et al.* [2015]. Figure 10 summarizes the findings
603 from *Shankar et al.* [2015] and this paper. In conclusion, these two papers have

604 advanced our understanding of the ecosystem dynamics of the NEAS from the
605 processes summarized in Figure 10a to those in Figure 10b.

606 We have demonstrated an example of coastal Kelvin waves influencing the
607 chlorophyll distribution in the NEAS. The coastal Kelvin waves generated in the
608 east coast of India drive a poleward coastal current (WICC) along the west coast
609 of India. This current advects low-salinity water to the NEAS and inhibits con-
610 vective mixing in the southern part of the NEAS. This inhibition of mixing, in
611 turn, inhibits the entrainment of nutrients into the ML and leads to low chloro-
612 phyll in the southern part compared to the northern part. However, horizontal ad-
613 vection of nutrients is not important. Our study shows that the growth rate of the
614 phytoplankton and even its physiology (N:P ratio) can be forced remotely. The
615 chronology of events that occur in the NEAS as a result of the inhibition of ML
616 deepening during the winter monsoon is as follows.

- 617 1. Entrainment of nutrients in the southern NEAS is inhibited by the inhibi-
618 tion of ML deepening. Hence, the southern NEAS is more limited by the
619 nutrients and is less productive compared to the northern NEAS. Addition-
620 ally, the bloom is sustained for a longer duration in the north.
- 621 2. The growth rate of phytoplankton is higher in the northern NEAS, owing
622 to the high nutrient limitation term, than in the south. The growth rate peaks
623 first in the southern NEAS in early January, and, roughly, a month later in
624 the north.
- 625 3. Owing to the contrasting growth rates, the N:P ratio of small phytoplank-
626 ton in the southern NEAS is higher than in the northern NEAS.
- 627 4. The inflow of low-salinity waters from the south inhibits not only the growth
628 of phytoplankton during the second half of the winter, but also the short-
629 lived detrainment bloom of large phytoplankton at the end of winter.

630 It is imperative that the findings from this study are further validated by fu-
631 ture observations in the NEAS; that should lead to a better understanding of the
632 ecosystem in the NEAS. It is expected that this paper will help to design such ex-
633 periments. Future observations should come up with measurements of the rates

634 of uptake of nutrients, rate of phytoplankton growth, rate of grazing, rate of rem-
635 ineralization, rate of sinking, etc., which will help to advance the modelling of
636 the ecosystem of the NEAS.

637 **Acknowledgments**

638 The authors thank K. Banse, an anonymous reviewer and S. B. Moran for their
639 critical evaluation of the manuscript. This work is a part of the High-resolution
640 Operational Ocean Forecast and reanalysis System (HOOFS) project of the In-
641 dian National Centre for Ocean Information Services (INCOIS), Ministry of Earth
642 Science, India and the Council of Scientific and Industrial Research (CSIR) OCEAN
643 FINDER programme. D. Shankar and A. C. Anil acknowledge funding from the
644 CSIR under the OCEAN FINDER programme. We acknowledge the Fund for
645 Improvement of S&T Infrastructure (FIST) of the Department of Science and Tech-
646 nology, Government of India and the Divecha Centre for Climate Change, Indian
647 Institute of Science (IISc), Bangalore for funding the high performance comput-
648 ing facility (Mandhan) at the Centre for Atmospheric and Oceanic Sciences, IISc,
649 Bangalore. The final simulation was carried out in SahasraT (CrayXC40) located
650 at the Supercomputer Education and Research Centre (SERC), IISc, Bangalore.
651 Analysis and visualisation were done using Ferret and the Generic Mapping Tools.
652 The data used in this paper are available from the sources listed in the support-
653 ing information (Tables S1, S3 and S4). This is CSIR-National Institute of Oceanog-
654 raphy contribution XXXX.

655 **References**

- 656 Amol, P., D. Shankar, S. G. Aparna, S. S. C. Shenoi, V. Fernando, S. R.
657 Shetye, A. Mukherjee, Y. Agarvadekar, S. Khalap, and N. P. Satelkar
658 (2012), Observational evidence from direct current measurements for
659 propagation of remotely forced waves on the shelf off the west coast
660 of India, *Journal of Geophysical Research: Oceans*, 117(C5), doi:
661 10.1029/2011JC007606, c05017.
- 662 Amol, P., D. Shankar, V. Fernando, A. Mukherjee, S. Aparna, R. Fernandes,
663 G. Michael, S. Khalap, N. Satelkar, Y. Agarvadekar, M. Gaonkar, A. Tari,

664 A. Kankonkar, and S. Vernekar (2014), Observed intraseasonal and sea-
665 sonal variability of the West India Coastal Current on the continental slope,
666 *Journal of Earth System Science*, 123(5), 1045–1074, doi:10.1007/s12040-
667 014-0449-5.

668 Anonymous (1965), Final cruise report of Anton Bruun cruises 4A and 4B,
669 International Indian Ocean Expedition, *Tech. rep.*, Woods Hole Oceanographic
670 Institution.

671 Antonov, J. I., D. Seidov, T. P. Boyer, R. A. Locarnini, A. V. Mishonov, H. E.
672 Garcia, O. K. Baranova, M. M. Zweng, and D. R. Johnson (2010), World
673 Ocean Atlas 2009, volume 2: Salinity, in *NOAA Atlas NESDIS 69*, edited
674 by S. Levitus, p. 184, U.S. Government Printing Office, Washington, D.C.

675 Balachandran, K., C. Laluraj, R. Jyothibabu, N. Madhu, K. Muraleedharan,
676 J. Vijay, P. Maheswaran, T. Ashraff, K. Nair, and C. Achuthankutty (2008),
677 Hydrography and biogeochemistry of the north western Bay of Bengal and
678 the north eastern Arabian Sea during winter monsoon, *Journal of Marine*
679 *Systems*, 73(12), 76 – 86, doi:10.1016/j.jmarsys.2007.09.002.

680 Banse, K. (1968), Hydrography of the Arabian Sea shelf of India and Pak-
681 istan and effects on demersal fishes, *Deep Sea Research and Oceanographic*
682 *Abstracts*, 15(1), 45 – 79, doi:10.1016/0011-7471(68)90028-4.

683 Banse, K. (1984), Overview of the hydrography and associated biological
684 phenomena in the Arabian off Pakistan, in *Marine geology and oceanography*
685 *of Arabian Sea and coastal Pakistan*, edited by J. D. Haq, B. U. Milliman,
686 pp. 271–303, Van Nostrand Reinhold, New York, National Institute of
687 Oceanography, Karachi.

688 Banse, K. (1987), Seasonality of phytoplankton chlorophyll in the central and
689 northern Arabian Sea, *Deep Sea Research Part A. Oceanographic Research*
690 *Papers*, 34(5-6), 713 – 723, doi:10.1016/0198-0149(87)90032-X.

691 Banse, K., and D. English (2000), Geographical differences in seasonality
692 of czcs-derived phytoplankton pigment in the arabian sea for 1978-1986,
693 *Deep Sea Research Part II: Topical Studies in Oceanography*, 47(78), 1623
694 – 1677, doi:10.1016/S0967-0645(99)00157-5.

695 Banse, K., and D. C. English (1993), Revision of satellite-based phytoplankton
696 pigment data from the Arabian Sea during the northeast monsoon, *Marine*
697 *Research*, 2 (1&2), 83 – 103.

698 Banse, K., and C. R. McClain (1986), Winter blooms of phytoplankton in
699 the Arabian Sea as observed by the Coastal Zone Color Scanner, *Marine*
700 *Ecology - Progress Series*, 34, 201 – 211.

701 Bonjean, F., and G. S. E. Lagerloef (2002), Diagnostic model and anal-
702 ysis of the surface currents in the tropical Pacific Ocean, *Journal*
703 *of Physical Oceanography*, 32(10), 2938–2954, doi:10.1175/1520-
704 0485(2002)032<2938:DMAAOT>2.0.CO;2.

705 Chatterjee, A., D. Shankar, S. S. C. Shenoi, G. V. Reddy, G. S. Michael,
706 M. Ravichandran, V. V. Gopalkrishna, E. P. Rama Rao, T. V. S.
707 Udaya Bhaskar, and V. N. Sanjeevan (2012), A new atlas of temperature
708 and salinity for the north Indian Ocean, *Journal of Earth System Science*,
709 121(3), 559–593, doi:10.1007/s12040-012-0191-9.

710 Chatterjee, A., D. Shankar, J. McCreary, and P. N. Vinayachandran (2013),
711 Yanai waves in the western equatorial Indian Ocean, *Journal of Geophysi-*
712 *cal Research: Oceans*, 118(3), 1556–1570, doi:10.1002/jgrc.20121.

713 Dickson, R. R., P. A. Gurbutt, and V. N. Pillai (1980), Satellite evidence
714 of enhanced upwelling along the European continental slope, *Jour-*
715 *nal of Physical Oceanography*, 10(5), 813–819, doi:10.1175/1520-
716 0485(1980)010<0813:SEOEUA>2.0.CO;2.

717 Dunne, J. P., R. A. Armstrong, A. Gnanadesikan, and J. L. Sarmiento (2005),
718 Empirical and mechanistic models for the particle export ratio, *Global*
719 *Biogeochemical Cycles*, 19(GB4026), doi:10.1029/2004GB002390.

720 Dunne, J. P., A. Gnanadesikan, J. L. Sarmiento, and R. D. Slater (2010),
721 Technical description of the prototype version (v0) of Tracers of
722 Phytoplankton with Allometric Zooplankton (TOPAZ) ocean bio-
723 geochemical model as used in the Princeton IFMIP model, *Biogeosciences*,
724 7(Suppl.):3593, [http://www.biogeosciences.net/7/3593/2010/bg-7-3593-](http://www.biogeosciences.net/7/3593/2010/bg-7-3593-2010-supplement.pdf)
725 2010-supplement.pdf.

726 Garcia, H. E., R. A. Locarnini, T. P. Boyer, J. I. Antonov, M. M. Zweng,
727 O. K. Baranova, and D. R. Johnson (2010), World Ocean Atlas 2009, vol-
728 ume 4: Nutrients (phosphate, nitrate, silicate), in *NOAA Atlas NESDIS 71*,
729 edited by S. Levitus, p. 398, U.S. Government Printing Office, Washington,
730 D.C.

731 Garcia, H. E., R. A. Locarnini, T. P. Boyer, J. I. Antonov, O. K. Baranova,
732 M. M. Zweng, J. R. Reagan, and D. R. Johnson (2014), World Ocean
733 Atlas 2013, volume 4: Dissolved inorganic nutrients (phosphate, nitrate,
734 silicate), in *NOAA Atlas NESDIS 76*, edited by A. Mishonov, p. 25, U.S.
735 Government Printing Office, Washington, D.C.

736 Geider, R. J., H. L. MacIntyre, and T. M. Kana (1997), A dynamic model
737 of phytoplankton growth and acclimation: Responses of the balanced
738 growth rate and chlorophyll a to carbon ratio to light, nutrient limitation
739 and temperature, *Marine Ecology Progress Series*, 148, 187–200.

740 Gnanadesikan, A., J. P. Dunne, and J. John (2011), What ocean biogeo-
741 chemical models can tell us about bottom-up control of ecosystem
742 variability, *ICES Journal of Marine Science*, 68(6), 1030–1044, doi:
743 10.1093/icesjms/fsr068.

744 Griffies, S. (2009), Elements of MOM4p1. GFDL ocean group,
745 *Tech. Rep. 6*, NOAA/Geophysical Fluid Dynamics Laboratory,
746 <http://www.gfdl.noaa.gov/>.

747 Griffies, S. M., and R. W. Hallberg (2000), Biharmonic friction with a
748 Smagorinsky-like viscosity for use in large-scale eddy-permitting ocean
749 models, *Monthly Weather Review*, 128(8), 2935–2946, doi:10.1175/1520-
750 0493(2000)128<2935:BFWASL>2.0.CO;2.

751 Han, W., J. P. McCreary, and K. E. Kohler (2001), Influence of precipi-
752 tation minus evaporation and Bay of Bengal rivers on dynamics, ther-
753 modynamics, and mixed layer physics in the upper Indian Ocean,
754 *Journal of Geophysical Research: Oceans*, 106(C4), 6895–6916, doi:
755 10.1029/2000JC000403.

756 Jain, V., D. Shankar, P. N. Vinayachandran, A. Kankonkar, A. Chatterjee,
757 P. Amol, A. M. Almeida, G. S. Michael, A. Mukherjee, M. Chatterjee,

758 R. Fernandes, R. Luis, A. Kamble, A. K. Hegde, S. Chatterjee, U. Das,
759 and C. P. Neema (2016), Evidence for the existence of Persian Gulf Water
760 and Red Sea Water in the Bay of Bengal, *Climate Dynamics*, pp. 1–20,
761 doi:10.1007/s00382-016-3259-4.

762 Klausmeier, C. A., E. Litchman, T. Daufresne, and S. A. Levin (2004), Opti-
763 mal nitrogen-to-phosphorus stoichiometry of phytoplankton, *Nature*, *429*,
764 171–174, doi:10.1038/nature02454.

765 Koné, V., O. Aumont, M. Lévy, and L. Resplandy (2009), Physical and bio-
766 geochemical controls of the phytoplankton seasonal cycle in the Indian
767 Ocean: A modeling study, in *Indian Ocean biogeochemical processes*
768 *and ecological variability*, pp. 147–166, American Geophysical Union,
769 doi:10.1029/2008GM000700.

770 Kurian, J., and P. N. Vinayachandran (2007), Mechanisms of formation
771 of the Arabian Sea mini warm pool in a high-resolution ocean general
772 circulation model, *Journal of Geophysical Research: Oceans*, *112*(C5),
773 doi:10.1029/2006JC003631, c05009.

774 Landry, M. R., S. L. Brown, L. Campbell, J. Constantinou, and H. Liu
775 (1998), Spatial patterns in phytoplankton growth and microzooplank-
776 ton grazing in the Arabian Sea during monsoon forcing, *Deep Sea Re-*
777 *search Part II: Topical Studies in Oceanography*, *45*(10), 2353 – 2368,
778 doi:10.1016/S0967-0645(98)00074-5.

779 Large, W. G., J. C. McWilliams, and S. C. Doney (1994), Oceanic vertical
780 mixing: A review and a model with a nonlocal boundary layer parameteri-
781 zation, *Reviews of Geophysics*, *32*(4), 363–403, doi:10.1029/94RG01872.

782 Lévy, M., D. Shankar, J.-M. André, S. S. C. Shenoi, F. Durand, and
783 C. de Boyer Montégut (2007), Basin-wide seasonal evolution of the In-
784 dian Ocean’s phytoplankton blooms, *Journal of Geophysical Research:*
785 *Oceans*, *112*(C12), doi:10.1029/2007JC004090, c12014.

786 Locarnini, R. A., A. V. Mishonov, J. I. Antonov, T. P. Boyer, H. E. Garcia,
787 O. K. Baranova, M. M. Zweng, , and D. R. Johnson (2010), World Ocean
788 Atlas 2009, volume 1: Temperature, in *NOAA Atlas NESDIS 68*, edited by
789 S. Levitus, p. 184, U.S. Government Printing Office, Washington, D.C.

790 Longhurst, A., and W. Wooster (1995), Abundance of oil sardine (*Sardinella*
791 *longiceps*) and upwelling on the southwest coast of India, *Canadian Jour-*
792 *nal of Fisheries and Aquatic Science*, 4(7), 2407 – 2419, doi:10.1139/f90-
793 268.

794 Madhupratap, M., S. P. Kumar, P. M. A. Bhattathiri, M. D. Kumar,
795 S. Raghukumar, K. K. C. Nair, and N. Ramaiah (1996), Mechanism of
796 the biological response to winter cooling in the northeastern Arabian Sea,
797 *Nature*, 384, 549 – 552, doi:10.1038/384549a0.

798 Marvasti, S., A. Gnanadesikan, A. A. Bidokhti, J. P. Dunne, and S. Ghader
799 (2015), Challenges in modelling spatiotemporally varying phytoplankton
800 blooms in the northwestern Arabian Sea and Gulf of Oman, *Biogeosciences*
801 *Discussions*, 12(13), 9651 – 9693, doi:10.5194/bgd-12-9651-2015.

802 McCreary, J. P., P. K. Kundu, and R. L. Molinari (1993), A numerical in-
803 vestigation of dynamics, thermodynamics and mixed-layer processes
804 in the Indian Ocean, *Progress in Oceanography*, 31(3), 181 – 244, doi:
805 10.1016/0079-6611(93)90002-U.

806 McCreary, J. P., K. E. Kohler, R. R. Hood, and D. B. Olson (1996), A four-
807 component ecosystem model of biological activity in the Arabian Sea,
808 *Progress in Oceanography*, 37(3-4), 193 – 240, doi:10.1016/S0079-
809 6611(96)00005-5.

810 McCreary, J. P., R. Murtugudde, J. Vialard, P. N. Vinayachandran, J. D.
811 Wiggert, R. R. Hood, D. Shankar, and S. Shetye (2009), Biophysical pro-
812 cesses in the Indian Ocean, in *Indian Ocean biogeochemical processes*
813 *and ecological variability*, pp. 9–32, American Geophysical Union, doi:
814 10.1029/2008GM000768.

815 Michaelis, L., and M. L. Menten (1913), Die kinetik der invertinwirkung
816 (The kinetics of invertase action), *Biochemische Zeitschrift*, 49, 333–369.

817 Morel, A., and D. Antoine (1994), Heating rate within the up-
818 per ocean in relation to its biooptical state, *Journal of Phys-*
819 *ical Oceanography*, 24(7), 1652–1665, doi:10.1175/1520-
820 0485(1994)024<1652:HRWTUO>2.0.CO;2.

821 Mysak, L. A., W. W. Hsieh, and T. R. Parsons (1982), On the relation-
822 ship between interannual baroclinic waves and fish populations in
823 the northeast Pacific, *Biological Oceanography*, 2(1), 63–103, doi:
824 10.1080/01965581.1982.10749453.

825 Naqvi, S., V. Sarma, and D. Jayakumar (2002), Carbon cycling in the north-
826 ern Arabian Sea during the northeast monsoon: significance of salps,
827 *Marine Ecology - Progress Series*, 226, 35 – 44.

828 Naqvi, S., P. Narvekar, and E. Desa (2006), Coastal biogeochemical pro-
829 cesses in the north Indian Ocean. Coastal segment (14,S-W), in *The Sea*,
830 vol. 14, edited by A. Robinson and K. Brink, chap. 19, pp. 723–781, Wiley,
831 Hoboken.

832 Naqvi, S. W. A., J. W. Moffett, M. U. Gauns, P. V. Narvekar, A. K. Pratihary,
833 H. Naik, D. M. Shenoy, D. A. Jayakumar, T. J. Goepfert, P. K. Patra, A. Al-
834 Azri, and S. I. Ahmed (2010), The Arabian Sea as a high-nutrient, low-
835 chlorophyll region during the late southwest monsoon, *Biogeosciences*,
836 7(7), 2091–2100, doi:10.5194/bg-7-2091-2010.

837 Park, J.-Y., and J.-S. Kug (2014), Marine biological feedback associated with
838 Indian Ocean Dipole in a coupled ocean/biogeochemical model, *Climate*
839 *Dynamics*, 42(1-2), 329–343, doi:10.1007/s00382-012-1640-5.

840 Park, J.-Y., J.-S. Kug, and Y.-G. Park (2014), An exploratory modeling study
841 on bio-physical processes associated with ENSO, *Progress in Oceanogra-*
842 *phy*, 124, 28 – 41, doi:10.1016/j.pocean.2014.03.013.

843 Pastor, M. V., J. B. Palter, J. L. Pelegr, and J. P. Dunne (2013), Physical
844 drivers of interannual chlorophyll variability in the eastern subtropical
845 north Atlantic, *Journal of Geophysical Research: Oceans*, 118(8), 3871–
846 3886, doi:10.1002/jgrc.20254.

847 Prasad, T. G., and M. Ikeda (2002a), A numerical study of the seasonal
848 variability of Arabian Sea high-salinity water, *Journal of Geophysical*
849 *Research: Oceans*, 107(C11), doi:10.1029/2001JC001139.

850 Prasad, T. G., and M. Ikeda (2002b), The wintertime water mass
851 formation in the northern Arabian Sea: a model study, *Journal*

852 *of Physical Oceanography*, 32, 1028–1040, doi:10.1175/1520-
853 0485(2002)032<1028:TWWMFI>2.0.CO;2.

854 Rochford, D. (1964), Salinity maxima in the upper 1000 m of the north In-
855 dian Ocean, *Australian Journal of Marine and Freshwater Research*, 15, 1
856 – 24.

857 Roy, R., and A. Anil (2015), Complex interplay of physical forcing and
858 prochlorococcus population in ocean, *Progress in Oceanography*, 137, Part
859 A, 250 – 260, doi:10.1016/j.pocean.2015.06.010.

860 Roy, R., R. Chitari, V. Kulkarni, M. Krishna, V. Sarma, and A. Anil (2015),
861 CHEMTAX-derived phytoplankton community structure associated with
862 temperature fronts in the northeastern Arabian Sea, *Journal of Marine*
863 *Systems*, 144, 81 – 91, doi:10.1016/j.jmarsys.2014.11.009.

864 Schott, F. A., and J. P. McCreary (2001), The monsoon circulation of
865 the Indian Ocean, *Progress in Oceanography*, 51(1), 1 – 123, doi:
866 10.1016/S0079-6611(01)00083-0.

867 Shankar, D., and S. R. Shetye (1997), On the dynamics of the Lakshadweep
868 high and low in the southeastern Arabian Sea, *Journal of Geophysical*
869 *Research: Oceans*, 102(C6), 12,551 – 12,562, doi:10.1029/97JC00465.

870 Shankar, D., P. Vinayachandran, and A. Unnikrishnan (2002), The monsoon
871 currents in the north Indian Ocean, *Progress in Oceanography*, 52(1), 63 –
872 120, doi:10.1016/S0079-6611(02)00024-1.

873 Shankar, D., R. Remya, P. N. Vinayachandran, A. Chatterjee, and A. Behera
874 (2015), Inhibition of mixed-layer deepening during winter in the northeast-
875 ern Arabian Sea by the West India Coastal Current, *Climate Dynamics*, pp.
876 1–24, doi:10.1007/s00382-015-2888-3.

877 Shenoi, S. S. C., D. Shankar, and S. R. Shetye (2004), Remote forcing an-
878 nihilates barrier layer in southeastern Arabian Sea, *Geophysical Research*
879 *Letters*, 31(5), doi:10.1029/2003GL019270, 105307.

880 Shetye, S., A. Gouveia, S. Shenoi, G. Michael, D. Sundar, A. Almeida, and
881 K. Santanam (1991), The coastal current off western India during the
882 northeast monsoon, *Deep Sea Research Part A. Oceanographic Research*

883 *Papers*, 38(12), 1517 – 1529, doi:10.1016/0198-0149(91)90087-V.

884 Shetye, S. R., S. S. Chandra Shenoi, M. K. Antony, and V. K. Kumar (1985),
885 Monthly-mean wind stress along the coast of the north Indian Ocean,
886 *Proceedings of the Indian Academy of Sciences - Earth and Planetary*
887 *Sciences*, 94(2), 129–137, doi:10.1007/BF02871945.

888 Shetye, S. R., A. D. Gouveia, S. S. C. Shenoi, D. Sundar, G. S. Michael,
889 A. M. Almeida, and K. Santanam (1990), Hydrography and circulation
890 off the west coast of India during the southwest monsoon 1987, *Journal of*
891 *Marine Research*, 48(2), 359–378, doi:10.1357/002224090784988809.

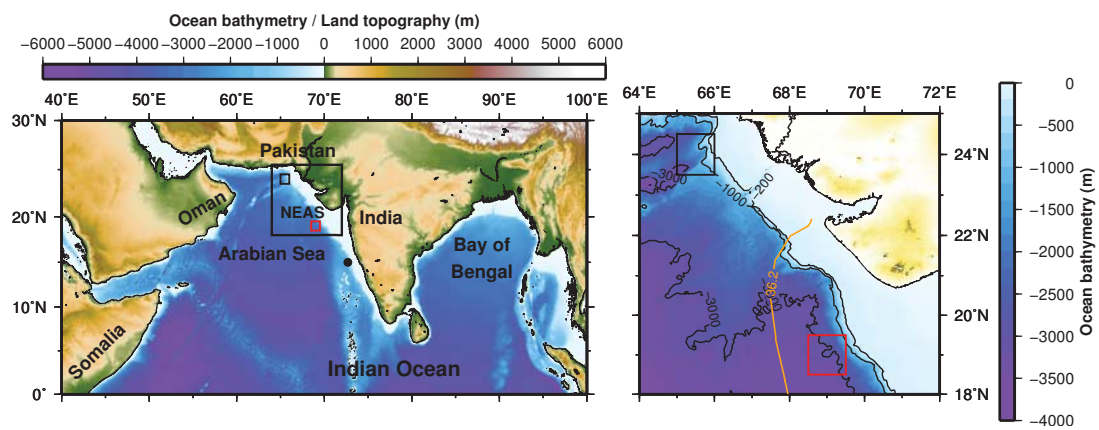
892 Shetye, S. R., I. Suresh, D. Shankar, D. Sundar, S. Jayakumar, P. Mehra,
893 R. G. Prabhudesai, and P. S. Pednekar (2008), Observational evidence for
894 remote forcing of the West India Coastal Current, *Journal of Geophysical*
895 *Research: Oceans*, 113(C11), doi:10.1029/2008JC004874.

896 Vialard, J., and P. Delecluse (1998), An OGCM study for the TOGA decade.
897 Part I: Role of salinity in the physics of the western Pacific fresh pool,
898 *Journal of Physical Oceanography*, 28(6), 1071–1088, doi:10.1175/1520-
899 0485(1998)028<1071:AOSFTT>2.0.CO;2.

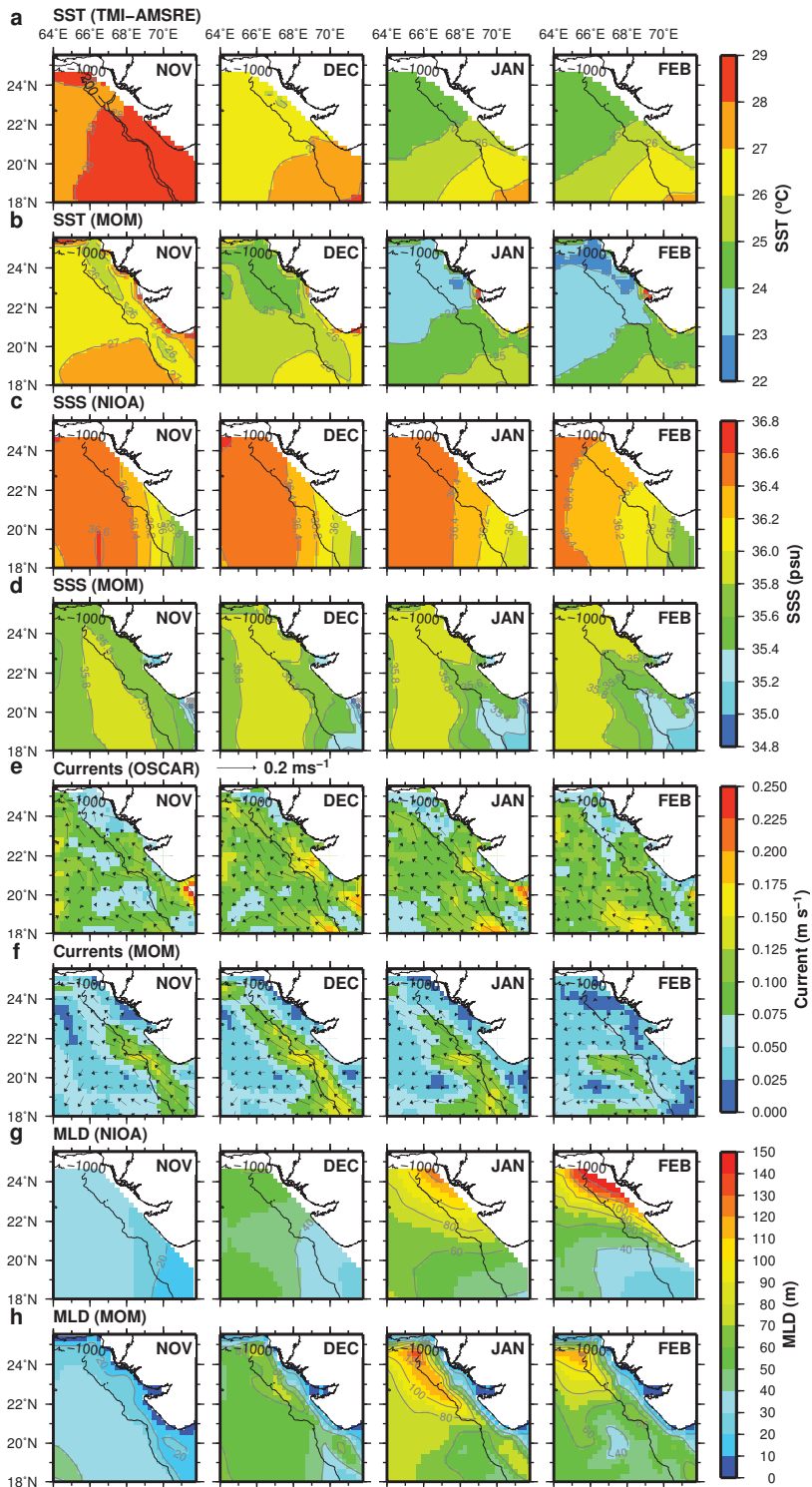
900 Vinayachandran, P. N., J. Kurian, and C. P. Neema (2007), Indian Ocean
901 response to anomalous conditions in 2006, *Geophysical Research Letters*,
902 34(15), doi:10.1029/2007GL030194.

903 Vôrôsmarty, C., B. Fekete, and B. Tucker (1996), River discharge database,
904 version 1.0 (rivdis vl. 0), *Tech. rep.*, UNESCO, Paris, France.

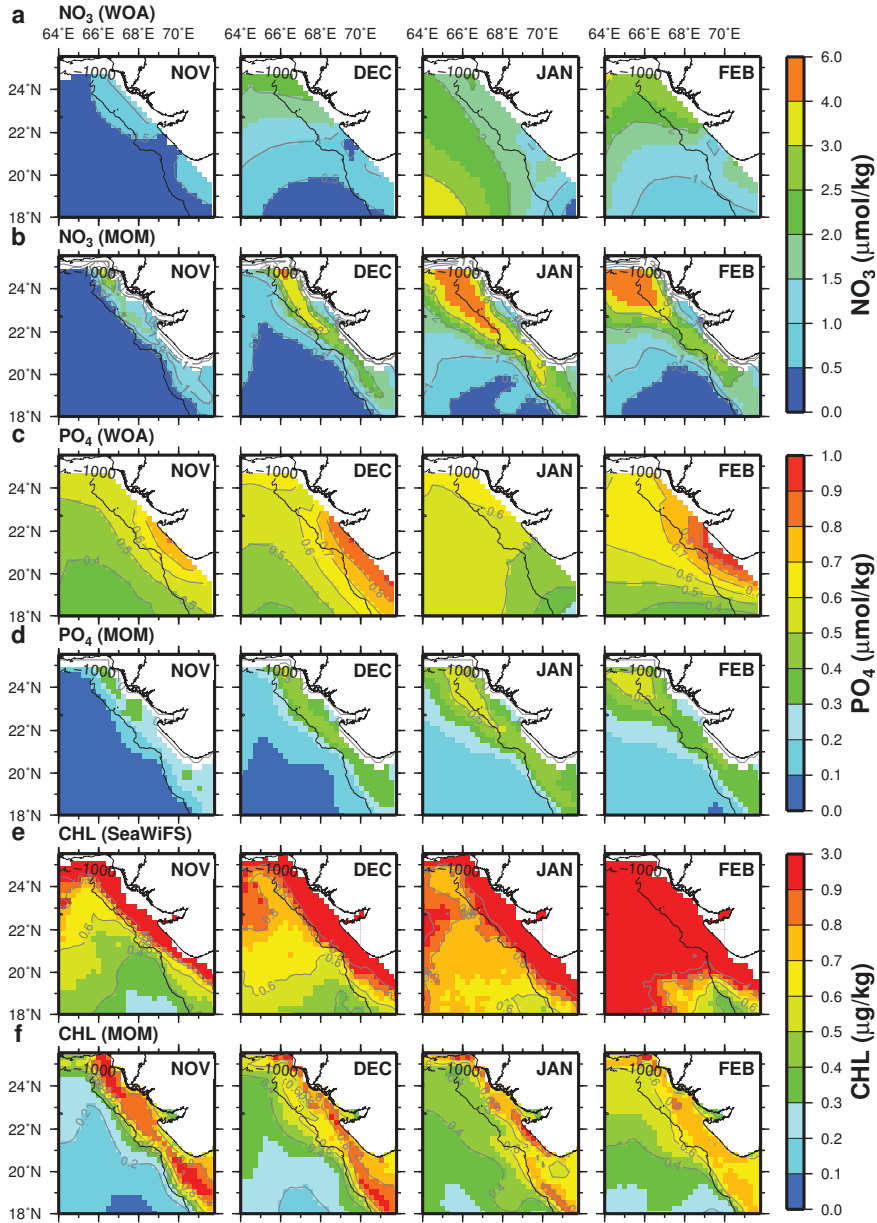
905 Wiggert, J., R. Murtugudde, and J. Christian (2006), Annual ecosystem
906 variability in the tropical Indian Ocean: Results of a coupled bio-physical
907 ocean general circulation model, *Deep Sea Research Part II: Topical Stud-*
908 *ies in Oceanography*, 53(5-7), 644 – 676, doi:10.1016/j.dsr2.2006.01.027.



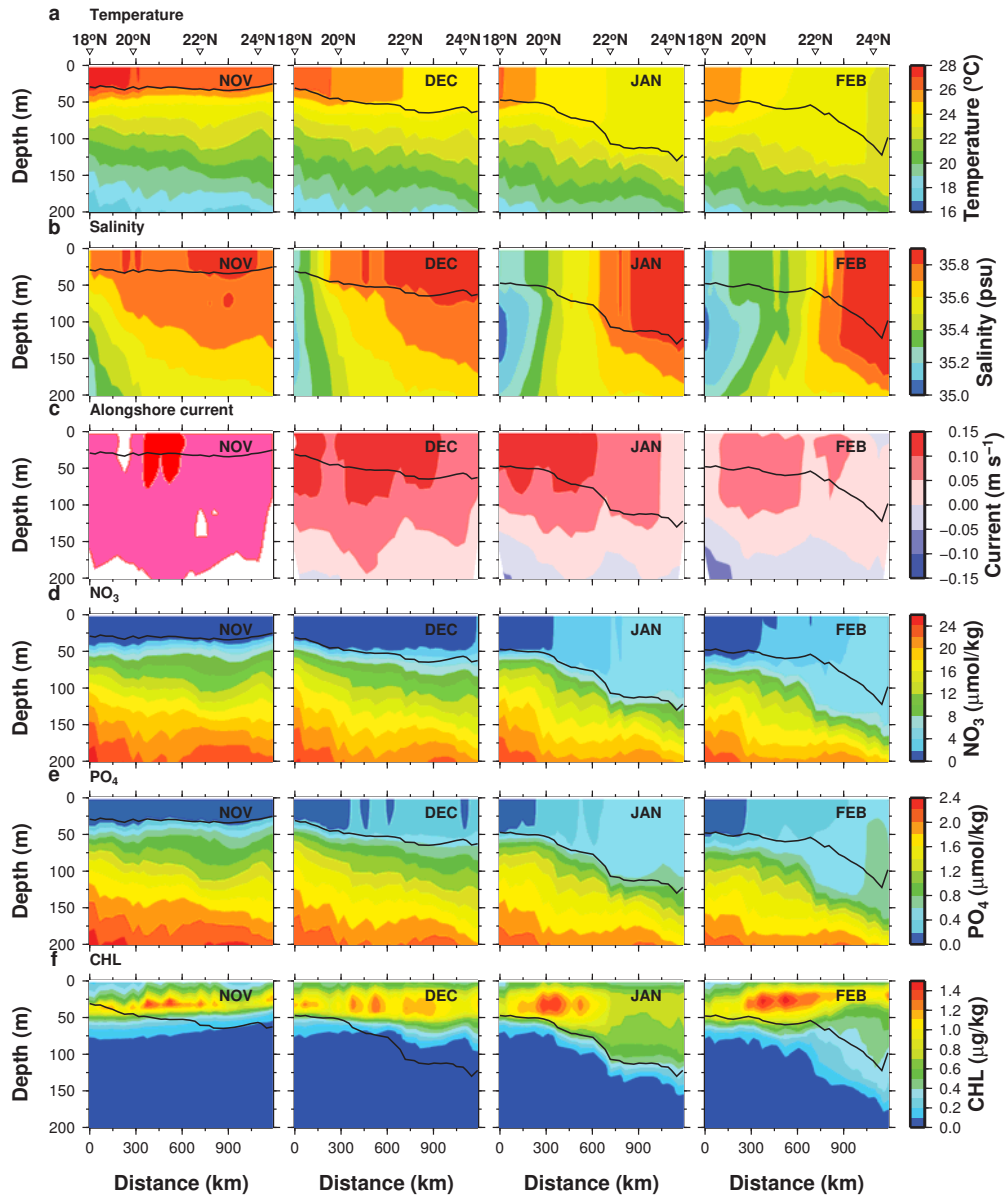
909 **Figure 1.** Map of the north Indian Ocean (left panel) and the northeastern Arabian Sea (right panel). Depth
 910 contours of 200 m and 1000 m are shown in the right panel. The salinity contour of 36.2 psu for February,
 911 drawn using the North Indian Ocean Atlas [Chatterjee *et al.*, 2012], is shown using an orange curve. The
 912 curve may be used as the boundary separating the northern and southern NEAS. Evolution of model variables
 913 is analysed in two $1^\circ \times 1^\circ$ boxes, shown in black and red colours, centred respectively at 65.5°E , 24°N and
 914 69°E , 19°N . The black dot in the left panel is referred to in Figure S2 in the supporting information. Ocean
 915 bathymetry and land topography are based on ETOPO-02.



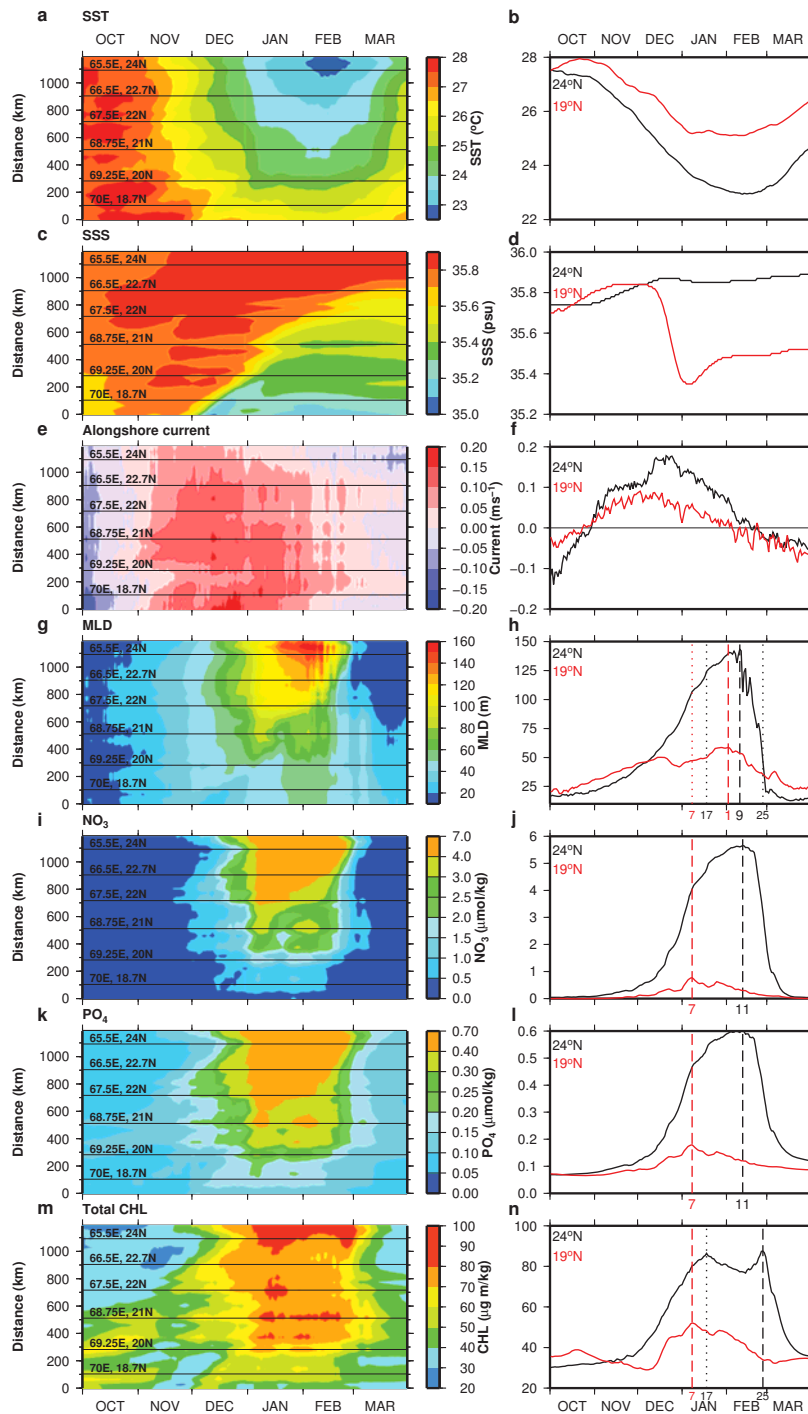
916 **Figure 2.** Monthly climatology of observed SST (a), modelled SST (b), observed SSS (c), modelled SSS
 917 (d), derived surface currents (e), modelled surface currents (f), observed MLD (g) and modelled MLD (h).
 918 Sources of each data set is indicated within parentheses on the top left corner of each row. Refer to the last
 919 paragraph of section 3 for details on data sources. The 1000 m isobath is marked.



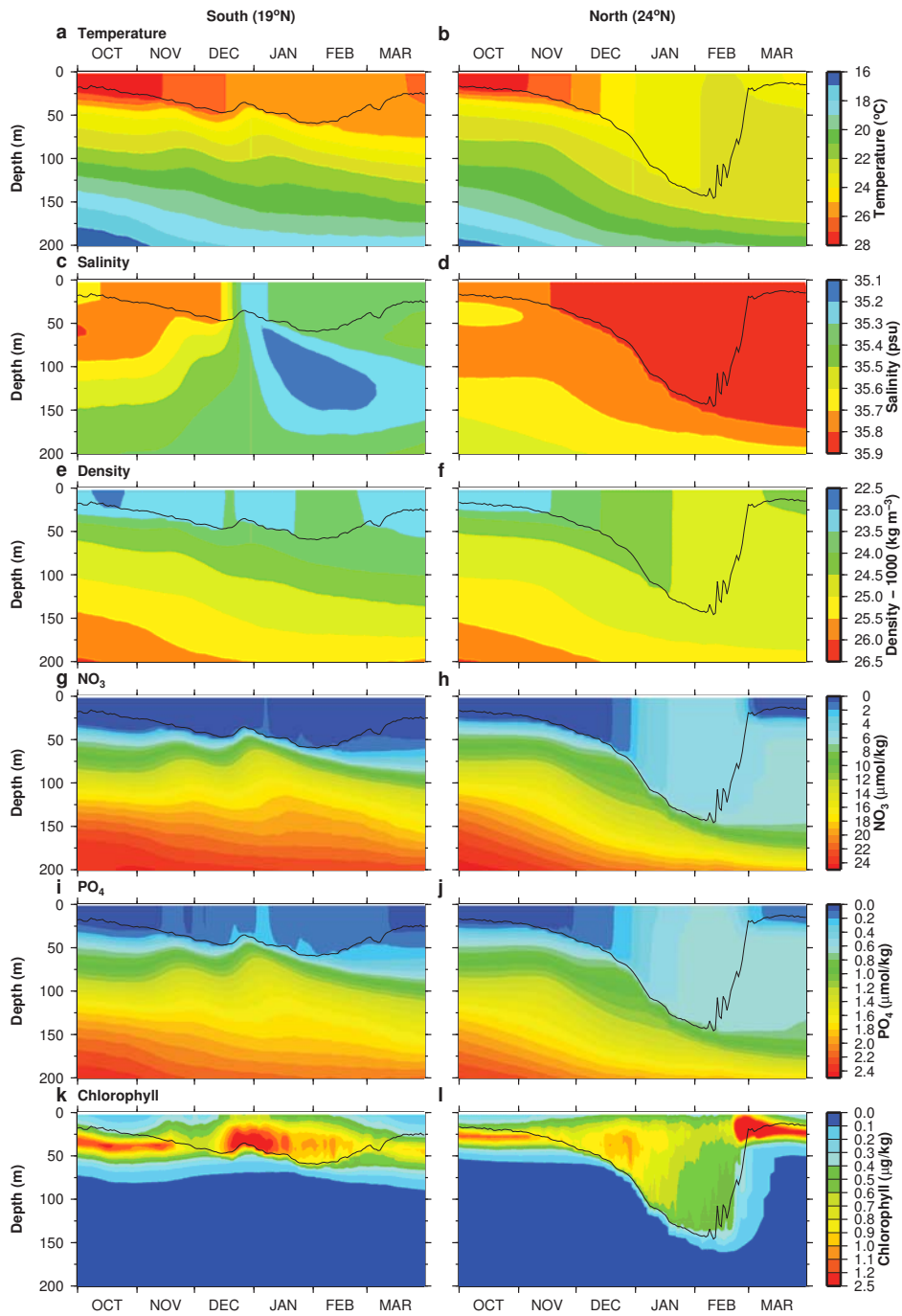
920 **Figure 3.** Monthly surface climatology of observed NO_3 (a), modelled NO_3 (b), observed PO_4 (c), mod-
 921 elled PO_4 (d), observed chlorophyll (e) and modelled chlorophyll (f). Sources of each data set is indicated
 922 within parentheses on the top left corner of each row. Refer to the last paragraph of section 3 for details on
 923 data sources. The 1000 m isobath is marked.



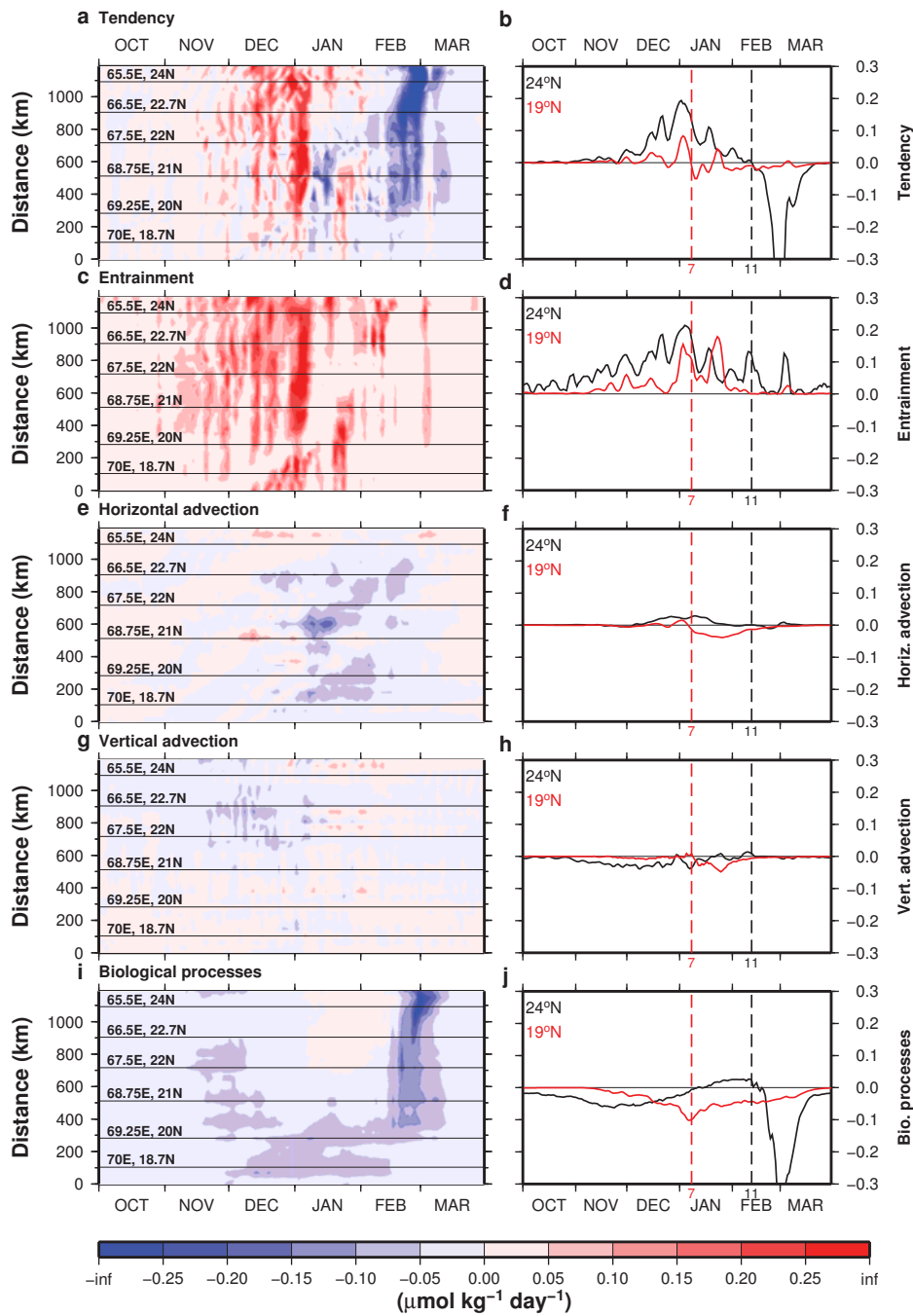
924 **Figure 4.** Monthly climatology of vertical sections of (a) temperature, (b) salinity, (c) alongshore current,
 925 (d) NO_3 , (e) PO_4 and (f) chlorophyll along the 1000 m isobath in the model. Black curve in each vertical
 926 section is the MLD.



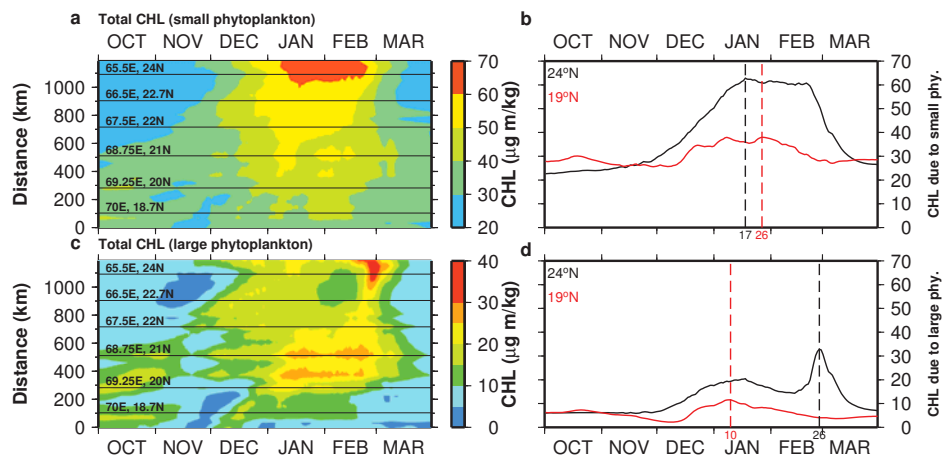
927 **Figure 5.** Time-series of (a and b) SST, (c and d) SSS, (e and f) alongshore current, (g and h) MLD, (i
 928 and j) surface NO_3 , (k and l) surface PO_4 and (m and n) depth integrated chlorophyll in the top 200 m water
 929 column. Panels on the left hand side show time series of variables along the 1000 m isobath. Panels on the
 930 right hand side show daily evolution of variables in the two boxes at 24°N and 19°N . In the right hand side
 931 panels, dashed vertical lines identify the peaks in each curve at 19°N (red) and 24°N (black). Dotted vertical
 932 lines identify either a secondary maximum or an event referred in the text. Dates of peak occurrence are given
 933 at the bottom of each panel.



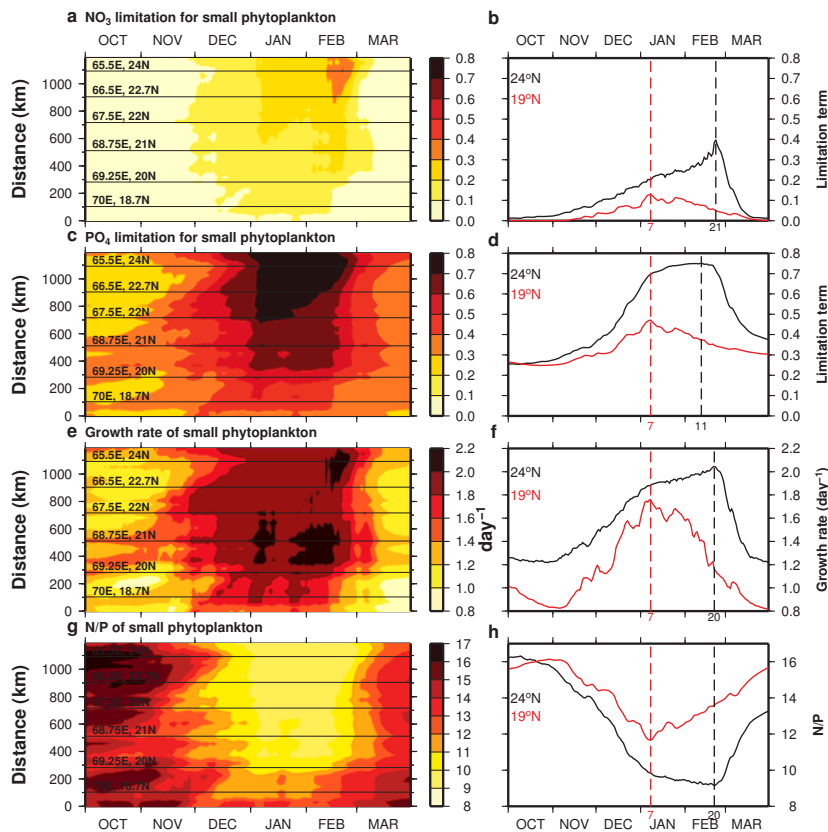
934 **Figure 6.** Temporal evolution of the vertical structure of (a and b) temperature, (c and d) salinity, (e and f)
 935 potential density, (g and h) NO_3 , (i and j) PO_4 and (k and l) chlorophyll at 69°E , 19°N and 65.5°E , 24°N .
 936 The black curve in each panel indicates evolution of ML. The panels on the left-hand side correspond to the
 937 southern location (19°N) and the panels on the right-hand side correspond to the northern location (24°N).
 938 The locations are shown in Figure 1.



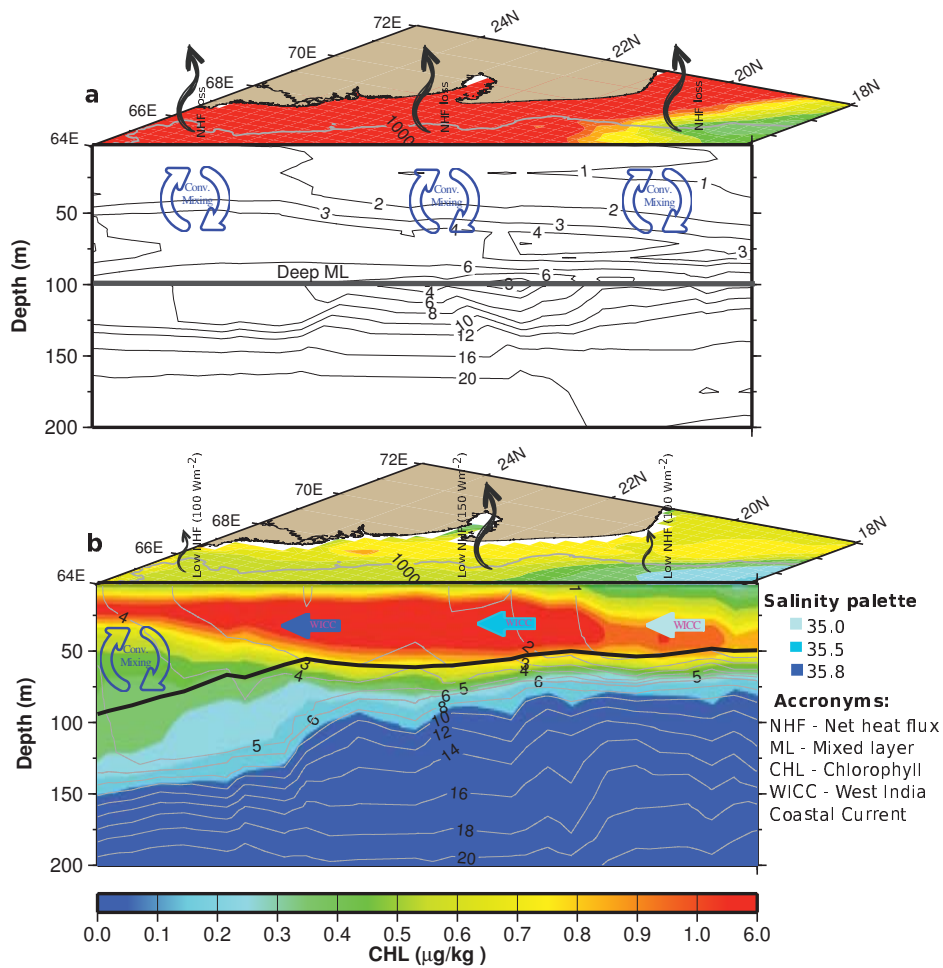
939 **Figure 7.** NO_3 budget in ML. Time-series of (a and b) tendency, (c and d) entrainment (e and f) horizontal
 940 advection, (g and h) vertical advection and (i and j) biological processes. Panels on the left hand side show
 941 the time-series along the 1000 m isobath. Panels on the right-hand side show evolution of variables in the two
 942 boxes at 24°N and 19°N . See Figure 1 for location of the boxes. Dashed vertical lines indicate the peaks of
 943 nitrate at 19°N (red) and 24°N (black). Dates of peak occurrence are given at the bottom of each panel.



944 **Figure 8.** Time-series of depth integrated chlorophyll in the top 200 m water column due to (a and b) small
 945 and (c and d) large phytoplankton. Panels on the left hand side show the time-series along the 1000 m isobath.
 946 Panels on the right hand side show evolution of variables in the two boxes at 24°N and 19°N. Dashed vertical
 947 lines indicate the peaks of small and large phytoplankton at 19°N (red) and 24°N (black). Dates of peak
 948 occurrence are given at the bottom of each panel.



949 **Figure 9.** Time-series of limitation terms for (a and b) NO₃ and (c and d) PO₄ for small phytoplankton,
 950 (e and f) growth rate of small phytoplankton and (g and h) N:P ratio of small phytoplankton at the surface
 951 level. Panels on the left hand side show the time-series along the 1000 m isobath. Panels on the right hand
 952 side show evolution of variables in the two boxes at 24°N and 19°N. Maxima and minima are indicated using
 953 dashed lines with corresponding dates given at the bottom.



954 **Figure 10.** (a) A schematic diagram illustrating the earlier understanding of dynamics of winter bloom in
 955 the NEAS. SeaWiFS climatology of chlorophyll for February is filled in the horizontal panel. The vertical
 956 panel shows contours of NO_3 along the 1000 m isobath during February available in *Garcia et al.* [2014]. A
 957 deep ML is indicated using a black line at a depth of 100 m. The three outward directed black arrows at the
 958 surface indicate net heat flux loss. Convective mixing is indicated using closed blue arrows in the ML. Note
 959 that the ML and net heat flux are not based on climatological data. (b) Summary of physical-biological pro-
 960 cesses in the NEAS as simulated by the model. Colours indicate concentrations of chlorophyll on the surface
 961 and in the vertical along the 1000 m isobath in February. Contours of simulated NO_3 along the 1000 m iso-
 962 bath during February is overlaid in the vertical section. ML is drawn using a black line. Poleward advection
 963 of low-salinity water by the WICC is marked using filled blue arrows.